ABSTRACT

PREDICTION OF FORELIMB MUSCLE ACTIVITIES AND MOVEMENT PHASES USING CORTICOSPINAL SIGNALS IN THE RAT

by
Sinan Gok

The targeted population for this project is primarily patients with high level spinal cord injury (SCI) and individuals with motor neuron diseases (MND). In both SCI and MND cases motor control is interrupted due to lack of communication between the brain and the musculature, although both sides are otherwise functional. The approach in this project is to use neural engineering techniques to restore the motor function that was lost because of an injury or disease.

Brain-computer interfaces (BCIs) attempt to extract the volitional signals from the cortex when the brain's normal outputs to the musculoskeletal system are impaired. However, BCIs that depend on the cortical activities suffer from two main impediments that are intrinsic to the BCI approach itself; firstly, under-sampling of the volitional information due to limited number of recording channels, and secondly, the long-term instability of the neuronal firings that make it difficult to track movement parameters, such as hand kinematics. As an alternative approach, a spinal cord computer interface (SCCI) can address both obstacles by providing means to access neural signals from a relatively smaller yet denser implant area in order to extract low-level movement parameters, such as muscle electromyography (EMG) signals, for prolonged signal stability. Since the descending fibers of the spinal cord influence the lower motor neurons that directly innervate the skeletal muscles, decoding the information in these fibers can provide a way

to establish a robust relationship between the neural control signals and the output parameter, that is the EMG signal.

The axons carrying the cortical information through the spinal cord are tightly bundled together in the descending tracts that eventually synapse with the inter-neurons and alpha motor neurons located in the spinal grey matter. The corticospinal tract (CST) is one of the descending tracts that carry the forelimb volitional information. In this study, the CST signals are recorded in rats that are implanted with custom-designed flexible multi-electrode arrays (MEAs). The power spectral density of the CST signals during the movement is notably higher than those observed during resting and anesthesia. The average inter-channel coherences up to 1.5 kHz are significantly higher for reach-to-pull task compared to face grooming and resting states, suggesting the presence of volitional information in the recorded CST signals. The results show that the CST signals can be segregated into two or three different classes using the forelimb movement components as guidance criteria with 97% and 71% accuracies, respectively. Predictions with correlation coefficients as high as 0.81 for the biceps EMG are achieved in individual sessions, although the average prediction accuracies vary considerably among rats. These results support the feasibility of an EMG-based Spinal Cord Computer Interface for patients with high level of paralysis.

PREDICTION OF FORELIMB MUSCLE ACTIVITIES AND MOVEMENT PHASES USING CORTICOSPINAL SIGNALS IN THE RAT

by
Sinan Gok

A Dissertation
Submitted to the Faculty of
New Jersey Institute of Technology
and Rutgers University Biomedical and Health Sciences – Newark
in Partial Fulfillment of the Requirements for the Degree of
Doctor of Philosophy in Biomedical Engineering

Department of Biomedical Engineering

May 2018

APPROVAL PAGE

PREDICTION OF FORELIMB MUSCLE ACTIVITIES AND MOVEMENT PHASES USING CORTICOSPINAL SIGNALS IN THE RAT

Sinan Gok

Dr. Mesut Sahin, Dissertation Advisor — Date
Professor of Biomedical Engineering, NJIT

Dr. Sergei Adamovich, Committee Member — Date
Professor of Biomedical Engineering, NJIT

Dr. Richard A. Foulds, Committee Member — Date
Professor Emeritus of Biomedical Engineering, NJIT

Dr. Stella Elkabes, Committee Member — Date
Associate Professor of Neurological Surgery, Rutgers New Jersey Medical School

---

Dr. Antje Ihlefeld, Committee Member — Date
Assistant Professor of Biomedical Engineering, NJIT

BIOGRAPHICAL SKETCH

Author: Sinan Gok

Degree: Doctor of Philosophy

Date: May 2018

Undergraduate and Graduate Education:

- Doctor of Philosophy in Biomedical Engineering,
  New Jersey Institute of Technology, Newark, NJ, 2018

- Master of Engineering in Electrical Engineering,
  Lehigh University, Bethlehem, PA, 2011

- Bachelor of Science in Electronics and Communication Engineering,
  Kocaeli University, Kocaeli, Turkey, 2006

Major: Biomedical Engineering

Presentations and Publications:

Gok, S. & Sahin M., 2018. Corticospinal activity can predict forelimb EMGs and movement components in the rat during the reach-to-pull task. Manuscript submitted for publication.

Guo, Y., Gok S. & Sahin M., 2018. Convolutional networks outperform linear decoders in predicting EMG from spinal cord signals. Manuscript submitted for publication.

Asan, A.S., Gok S. & Sahin M., 2018. Electric fields induced by transcutaneous and intracranial current injections in the rat brain. *Proceedings of the 40th Annual International Conference of the IEEE Engineering in Medicine and Biology Society (EMBS)*, Honolulu, HI. Manuscript accepted for publication.

Cetinkaya, E., Gok S. & Sahin M., 2018. Carbon fiber electrodes for *in vivo* spinal cord recordings. *Proceedings of the 40th Annual International Conference of the IEEE Engineering in Medicine and Biology Society (EMBS)*, Honolulu, HI. Manuscript accepted for publication.

Cetinkaya, E., Gok S. & Sahin M., 2017. Carbon fiber electrodes for recording spinal cord activity in rats. Poster presented at the *Biomedical Engineering Society (BMES) Annual Meeting*, Phoenix, AZ.

Gok, S. & Sahin M., 2017. Rat forelimb movement components segregated by corticospinal tract activity. *Proceedings of the International IEEE/EMBS Conference on Neural Engineering, (NER)*, pp. 312–315.

Gok, S. & Sahin M., 2016. Prediction of forelimb muscle EMGs from the corticospinal signals in rats. *Proceedings of the 38th Annual International Conference of the IEEE Engineering in Medicine and Biology Society (EMBS)*, vol. 2016–October, pp. 2780–2783.

Gok, S. & Sahin M., 2016. Predicting forelimb muscle activity from corticospinal signals in rats. Poster presented at the *International Brain Computer Interface Meeting*, Pacific Grove, CA.

Gok, S., Charkhkar, H., Pancrazio J. & Sahin, M., 2015. In vivo impedance characterization of PEDOT:TFB coated and chronically implanted multi-electrode arrays. Poster presented at the *Biomedical Engineering Society (BMES) Annual Meeting*, Tampa, FL.

Gok, S. & Sahin, M., 2014. A method of chronic neural recording from rat corticospinal tract using flexible multi-electrode arrays. Poster presented at the *41st Neural Interface Conference*, Dallas, TX.

To my wife, Birsu.

ACKNOWLEDGEMENT

I must express my very profound gratitude to Dr. Mesut Sahin, my dissertation advisor. This work would not have been possible without his guidance, support, and encouragement.

I would like to thank Dr. Sergei Adamovich, Dr. Richard A. Foulds, and Dr. Antje Ihlefeld from NJIT and Dr. Stella Elkabes from Rutgers NJMS for serving in my dissertation committee and their valuable contributions into my research.

I would also like to thank current and former members of the Neural Prosthetics Laboratory: Ferhat Erdogan, Ahmet Asan, Esma Cetinkaya, Ozan Cakmak, and Dr. Ali Ersen for giving me the motivation and emotional support I needed to finish my work.

Finally, I would like to thank my parents, whose love and good wishes are with me wherever I go.

TABLE OF CONTENTS

TABLE OF CONTENTS
(Continued)

Chapter **Page**

TABLE OF CONTENTS
(Continued)

LIST OF TABLES

LIST OF FIGURES

LIST OF FIGURES
(Continued)

LIST OF FIGURES
(Continued)

LIST OF FIGURES
(Continued)

LIST OF FIGURES
(Continued)

Figure **Page**

CHAPTER 1

INTRODUCTION

1.1 Problem Significance

Individuals with Motor Neuron Diseases (MNDs) and Spinal Cord Injury (SCI) suffer from motor deficits because the communication between the nervous system and the musculature has been severely interrupted or entirely cut off. MNDs describe the condition where the muscle control is disrupted due to the damage to the nervous system as a result of a disease, such as Amyotrophic Lateral Sclerosis (ALS). Spinal cord injury (SCI) refers to a damage to the spinal cord mainly caused by a trauma, such as motorcycle accident. In addition to motor deficits, these conditions are associated with many physical impairments including, respiratory, urinary, gastrointestinal, and sexual problems as well as psychological side effects such as depression and anxiety.

The annual incidence of SCI is recently estimated as 54 cases per million population in the US, which translates to approximately 17,000 new cases each year (National Spinal Cord Injury Statistical Center 2017). This number is believed to be 250,000 - 500,000 per year worldwide (World Health Organization 2016). Depending on the individual's age and level of the injury, life expectancy ranges between 7.9 and 53.4 years for persons who survived at least 1-year post injury (National Spinal Cord Injury Statistical Center 2017) and the estimated lifetime costs in the US ranges from 2.1 to 5.4 million dollars (Cao et al. 2011). The most common site of injury is at the cervical level (C1-C4), resulting tetraplegia. These patients' life quality can be significantly improved by providing alternative ways of voluntary command generation in order to better take care of themselves.

1.2 Innovation

Brain computer interfaces (BCI) aim to extract the movement intentions from the cortex when brain's normal connections to the musculoskeletal system are impaired (Wolpaw et al. 2000). The most common method of extracting movement information from the brain is to record spiking activities of primary motor neurons (Hochberg et al. 2006; Lebedev & Nicolelis 2006; Serruya et al. 2002; Taylor et al. 2002; Nicolelis 2003). In this method, a penetrating electrode is inserted a few millimeters down into the cortex, ideally close to neurons that fire in conjunction with the desired movement (Nicolelis 2003). To increase the number of the neurons that are being sampled, microelectrode arrays with up to several hundred recording tips are preferred (Suner et al. 2005).

Despite the successes that current BCI technologies have presented until today, they suffer from two main impediments that are inherent to the BCI approach itself: firstly, only a limited number of cortical neurons are sampled, which does not contain sufficient representation of the movement. To obtain a true representation, the spatial resolution of the neural interface must be sufficiently large (Schwartz et al. 2006). Secondly, due to a variety of reasons, including tissue encapsulation around the electrode tip and subsequent neuronal cell death (Vadim S. Polikov et al. 2005; Saxena et al. 2013) and the change in neurons' firing preferences (Kurtzer et al. 2005), the neurons of interest become unavailable in long term applications. Consequently, tracking neurons that are correlated with a high-level movement parameter, such as hand kinematics and direction, becomes increasingly harder.

The aforementioned obstacles undermine the reliability of the BCI systems. As an alternative approach, a spinal cord computer interface (SCCI) can address both obstacles

by providing means to access neural signals from a relatively smaller but denser implant area while tracking a low-level movement parameter, such as the muscle electromyography (EMG), for prolonged signal stability. In the SCCI approach, the targeted structures are the descending pathways that carry the modulated control signals from the supraspinal structures to the spinal cord neurons. The movement parameter is the muscle EMG which also tracts the spinal cord output. If one can figure out the relationship between the descending signals and the spinal cord output signals, a more robust system can ultimately be built for extraction of the volitional signals from the CNS.

1.3 Current Challenges in BCI Technology

BCIs track spiking activity of single cells to extract volitional signals. As shown in recent studies, monkeys were able to feed themselves through cortical control of a robotic arm (Velliste et al. 2008). As for human studies, it has been reported that tetraplegic patients were able to move a computer cursor to open and close a prosthetic hand using neural ensembles (Hochberg et al. 2006; Truccolo et al. 2008). Despite all these impressive advances in M1-based BCIs there are unresolved challenges that need to be addressed. For instance, several studies have shown that the information related to the movement is encoded in multiple brain areas (Kalaska et al. 1997; Wessberg & Nicolelis 2004; Santucci et al. 2005a), which is termed as "distributed coding principle" (Nicolelis & Lebedev 2009). To obtain the full representation of the movement, one has to implant many electrodes in multiple brain areas; a task that implies a high degree of surgical risk for the patient. Another challenge is that the prediction accuracy of a BCI depends not only on the number of neurons being recorded from but also the movement parameter that is reconstructed (Carmena et al. 2003). Thus, recording from individual neurons whose

functions are highly correlated with a suitably selected set of tasks can be misleading since it disregards all the other potential modes of movement (Fetz 1992). Furthermore, relying on the activity of individual neurons may not be a robust approach since a single neuron has limited information content and exhibits a stochastic firing behavior, and thus the focus in BCI research has shifted to "neuronal population activity" (Averbeck et al. 2006). It is hard to track the same neurons since the electrode tips are susceptible to micro-motions and glial encapsulations, whereas the population vector from a large number of cells is more resilient to the movement of the electrodes.

1.4 Spinal Cord Computer Interfacing

To address the challenges associated with contemporary BCI technologies, our group has proposed accessing the spinal cord descending tracts to extract the movement related volitional signals as an alternative method (Prasad & Sahin 2006). Since the encoded movement information has to travel through the spinal cord, tapping into descending signals at the spinal level may provide access to sufficient volitional information within a relatively smaller implant area.

The spinal cord contains two major descending systems: the lateral and the medial systems. The medial descending system is mainly involved in posture related activities by integrating vestibular, visual, and somatosensory information (Squire et al. 2008). The lateral system consisting of the corticospinal tract (CST) and the rubrospinal tract (RST) is involved in producing skilled forelimb movements and constitutes the main pathways for motor control in mammals (Gibson et al. 1985; Iwaniuk & Whishaw 2000). Electrophysiological lesion studies showed that the RST and CST have equal importance in forelimb control, although the relative contributions vary across species. Unilateral

lesions to red nucleus, from which the RST originates, and medullary pyramid impaired the rotatory movements in rats including limb aiming, pronation and supination (Whishaw et al. 1998). Impaired arpeggio movement in some lesioning studies (Whishaw et al. 1998; Morris et al. 2011) suggest that the rat RST is more involved in proximal movements (e.g., hand rotation) than in digit use. On the other hand, it has been shown that rat's ability to orient the paw for reaching was diminished following selective CST lesions, expressing a similarity to human CST injury (Carmel et al. 2010). In summary, the current research suggests involvement of both the RST and CST in forelimb control, although the significance of each may be different depending on the specie and the behavioral task.

Figure 1.1 shows the position of RST and CST in the spinal white matter. In rats, the CST is located in the ventral most portion of the dorsal column of the spinal white matter (Sengul & Watson 2014). The majority of CST fibers originates from primary the motor cortex and the primary somatosensory cortex. They mainly terminate in the medial part of the dorsal horn and the intermediate gray matter, namely Rexed's laminae 3, 4, 5, and 6 (Sengul & Watson 2015).

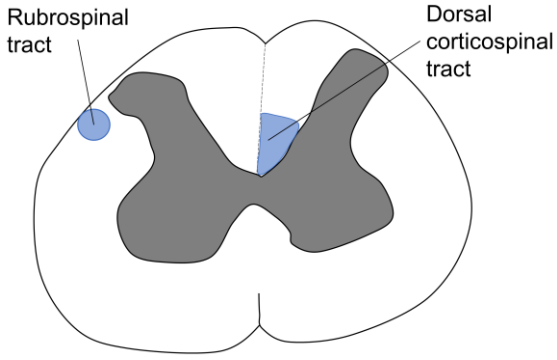

Figure 1.1 The lateral descending pathways in the rat spinal cord. The RST lies ventral to the junction of the dorsal horn, whereas the CST is located in the ventral most portion of the dorsal column of the white matter. Both tracts descend contralateral to their origin.

The number of fiber counts in the cervical spinal cord ranges between 69,000 and 137,000 depending on the segmental level and whether light or electron microscopy is used (Brown 1971; Gorgels et al. 1989; Gorgels 1990; Leenen et al. 1989). In adult rats, about two thirds of those fibers are myelinated. In medullary pyramid, the fiber diameter varies between 0.1 μm and 4.92 μm, most of which are slow conducting fibers with diameters less than 1 micron (Gorgels 1990; Dunkerley & Duncan 1969; Leenen et al. 1985). The conduction velocities of CST fibers were reported to be in the range of 5-19 m/s (Alstermark et al. 2004; Mediratta & Nicoll 1983). The cross sectional area of CST in mid-cervical level is about 0.08 mm^2 (Dunkerley & Duncan 1969). By tapping into the intact regions of the cervical spinal cord above the injury point, a spinal cord-computer interface can be built for voluntary command generation.

The participation of CST in distal muscle control is prominent in non-human primates (Kuypers 1964; Nakajima et al. 2000) and humans (de Noordhout et al. 1999), which makes it an ideal site to extract volitional information for BCI applications. Even though the direct corticospinal projections to forelimb motoneurons are sparse in non-primate mammals, such as the cat (Kuypers 1981) and the rat (Alstermark et al. 2004; Yang & Lemon 2003), evidence suggests an indirect involvement of the CST in forelimb movements through interneuronal pools of the spinal segment. For instance, experiments in cats have shown that corticospinal excitation can influence the spinal motor neurons indirectly through the propriospinal pathways (Alstermark et al. 1984; Illert & Lundberg 1978). Therefore, investigating the role of CST in voluntary command generation in rats may provide insights into the feasibility of CST-based neural interfaces.

After an injury that severs the spinal cord, the proximal motor fibers in the spinal cord remain functional (Pruitt et al. 1988). By tapping into the intact regions of the cervical spinal cord above the point of injury, a Spinal Cord Computer Interface can be built for voluntary command generation. Our group has reported the ability to reconstruct forelimb kinematics, such as hand velocity and elbow angle, using neural signals recorded from rat CST by the penetrating Utah multielectrode arrays (MEAs) and micro-wires (Prasad & Sahin 2012a). Our group has also demonstrated that forelimb isometric forces (Guo et al. 2014) can be predicted using CST signals recorded with ECoG type flexible MEAs. Based on these findings, the CST is chosen as the primary recording site in this study.

1.5 CST Following the Spinal Cord Injury

SCCI approach relies on the information extracted from the CST that is proximal to injury site. However, whether or not the CST neurons and axons survive the SCI has been a subject of debate for many years. One of the commonly used methods to detect surviving cells was retrograde labeling by injecting horseradish peroxidase (HRP) above the injury. Using HRP labelling, Feringa et al. observed cell death in spinal (transected at T6/T7) rats 5 and 10 weeks after injury, which progressively continued for at least 25 weeks following the injury (Feringa et al. 1983). In a follow-up study, Feringa and Vhalsing used the same labelling on T9 transected rats and observed that only 7% of cortical neurons projecting to the spinal cord matched the neurons labelled in the control group (Feringa & Vahlsing 1985). Lee et al. observed that after a contusion injury at T9 in rats, the latencies of measured motor evoked potentials (MPEs) were lengthened and their amplitudes were lowered. The authors suggested that, along with the behavioral changes, the lengthened latencies indicate cell death in sensorimotor cortex following SCI (Lee et al. 2004). After

SCI in monkeys, apoptotic cell death was observed in the white matter away from the injury site and attributed to the demyelination in the fiber tracts (Crowe et al. 1997). Finally, Hains et al. claimed that at least 40% of identified CST neurons (the cortical neurons that project via the CST pathway) underwent apoptosis 1 week after the injury and a significant portion of cells were lost after 2 weeks (Hains et al. 2003). Despite these studies warning against apoptosis and demyelination after SCI, at least an equal number of studies proved the contrary. In follow up studies, Nielson et al replicated Hains' experiment and failed to show evidence of loss of CST axons in the medullary pyramid eliminating the possibility of extensive apoptotic cell death (Nielson et al. 2011). McBride et al. used retrograde labeling with Fluro-Gold following T9 transection in the rats and observed that the number of labeled corticospinal and rubrospinal neurons did not change after a new T1 transection followed by Fluro-Gold injection (McBride et al. 1990). More notably, Barron et al. compared spinal rats (transected at T7) sacrificed at 10 weeks post-injury with a control group and observed no indication of cell death after light and electron microscopic studies (Barron et al. 1988). And finally, Pruitt et al. reported a decrease in the volume of the CST in rats 10 weeks after complete T9 transection, but observed no loss in the number of axons in CST at C2 and T1 levels (Pruitt et al. 1988). These studies indicate that a substantial amount of CST axons do survive after spinal cord injury and lay the foundations for a spinal cord computer interface.

1.6 Kinematic vs. Kinetic Movement Parameters

Historically, decoding kinematic parameters (hand position and velocity, joint angle, etc.) from the activity of primary motor cortex (M1) neurons has been the primary method in BCI research. Evarts first showed that the firing pattern of individual pyramidal tract

neurons (PTN) is correlated with the spontaneous movement of the arm in monkeys (Evarts 1966). Later, his experiments on behaving monkeys revealed that firing of most PTNs was mainly associated with force (Evarts 1968). In the following years, it was reported that neural discharge was also correlated with the direction of the movement (Georgopoulos et al. 1982), hand position and velocity (Paninski et al. 2004), and joint angle (Vargas-Irwin et al. 2010). However, BCI models that depend on kinetic parameters, such as electromyography (EMG), rather than kinematic parameters, such as hand direction and joint angle, have the ability to adapt changing conditions more efficiently. Cherian et al. have compared the performances of BCIs with kinetic (EMG) and kinematic (position and velocity) outputs using M1 recordings in monkeys (Cherian et al. 2011) and reported that EMG decoders generalized better than kinematic recorders under varying task conditions. Ultimately, biologically realistic BCIs will rely on both kinematic and kinetic parameters, since neuromuscular system modulates the biomechanical properties of the limbs to naturally interact with the environment. Thus, it is important to address the relationship between the cortical signals and the muscle activities during volitional movements.

1.7 Objectives

The primary objective of this project was to utilize flexible microelectrode arrays (MEAs) to record movement related volitional signals from one of the lateral descending tracts of the rat spinal cord, the corticospinal tract (CST), with the expectation of reduced tissue response, compared to other electrodes used by our group in the past, and increased signal stability. The CST pathways carry the motor signals from the brain to the spinal cord neuronal circuitry that ultimately controls distal muscles. Tapping into descending signals at the spinal level may provide access to sufficient information encoding the voluntary

movements within a relatively smaller implant area. The following three aims were designed to characterize the descending signals recorded from the rat CST, demonstrate their use as command signals for forelimb control, and evaluate the tissue response caused by the electrode implants.

1.7.1 Aim 1: Chronic Recordings from the CST during a Skilled Reaching Task

The aim was designed to demonstrate the quality and long-term stability of the signals recorded with chronically implanted multi-electrode arrays. A custom designed MEA with a thickness of 12 µm and a width of 600 µm was implanted in the rat CST and neural signals were recorded. The recorded signals were evaluated based on their information content and long-term stability. For this purpose, five Long Evans rats were trained to perform a reach-to-pull task. After training was completed, rats were underwent survival surgery for electrode implantation. Dorsal laminectomy was performed and the MEA was inserted down vertically along the central fissure of the cord into the dorsal column at the C4 level, i.e. the CST controlling the ipsilateral arm. The array captured multi-spiking activity from a dense population of axons in the CST. The variations in the signals due to the micro-motions were expected to be minimal. The predefined contact configuration of the electrode array allowed us to correlate the neural activity with the contact positions in the array and track them longitudinally throughout the implant period.

1.7.2 Aim2: Studying the Correlation between CST Signals and Forelimb Movements

This aim was designed to outline the relationship between the CST signals and the different aspects of the forelimb movements. The force signal and electromyography (EMG) signals from various forelimb muscles were simultaneously recorded along with the CST signals

during a reach-to-pull task. Two supervised machine learning techniques, classification and regression, were used in data analysis. The approach followed in this aim was to extract features from the CST signals, show that they are correlated with different aspects of the forelimb movement, and use supervised learning algorithms to accurately model the relationship between the CST and forelimb movements. By examining the force profiles and electromyographic (EMG) signals from various forearm muscles (wrist extensors and flexors, biceps, and triceps), the forelimb movement was divided into two (reaching and pulling) and three (wrist extension, wrist flexion, and grasping) components to be used in two different classification paradigms. The degree of success in segregating these components was determined by the ratio of the number of the correct classifications to the total number of classifications. The CST signals were also used for EMG prediction in which the correlation coefficient and coefficient of determination were used as the measures of prediction success.

1.7.3 Aim 3: Histological Examination of the MEA Implants

This aim was designed to provide insights into the immune response of the spinal cord induced by the electrode implantation. For histological evaluation, rats were sacrificed and perfused after the electrophysiological data for the above two aims were collected, which took about 4 to 8 weeks. Tissue was dissected from each animal and taken to a core laboratory for immunohistological analysis. The spinal cord samples from the implanted spinal cord area were sectioned and stained with Haemotoxylin and Eosin (H&E) and Luxol Fast Blue (LFB, myelin marker). A qualitative discussion of the histological response to the electrode implants will be presented.

CHAPTER 2

EXPERIMENTAL DESIGN

2.1 Materials and Methods

2.1.1 Custom Designed Flexible Microelectrode Array

A custom designed planar electrode array (NeuroNexus, MI) was used as the neural recording electrode in this study. The array consisted of 27 platinum (Pt) contacts with 25 µm diameter. Contacts were in a 4x7 configuration with a 80 µm vertical and 100 µm horizontal inter-contact spacing, occupying an area of about 300 µm x 600 µm with two large reference contacts on each side (Figure 2.1). The electrode substrate was a 600 µm-wide polyimide ribbon cable with a thickness of 12 µm. The external connection was made through a plastic micro connector (Omnetics, MN).

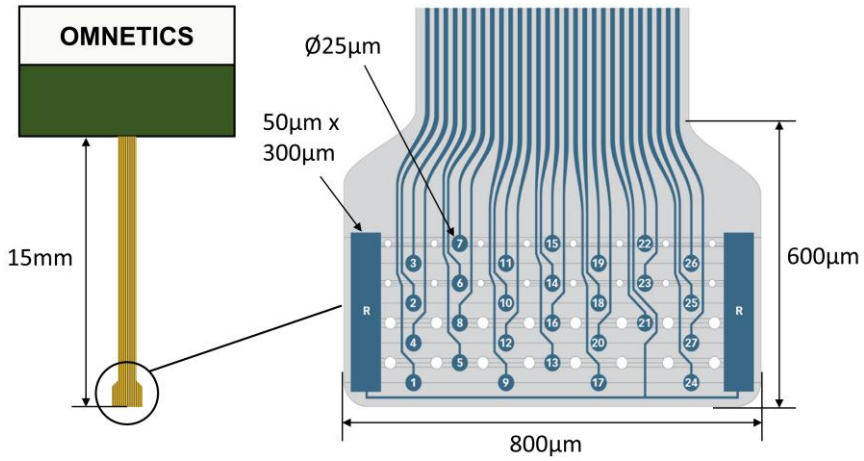

Figure 2.1 The custom made flexible microelectrode array (NeuroNexus, MI) and the dimensions of the electrode tip.

2.1.2 Training and Recording Box

A clear plexi-glass box with a 3x1 cm vertical opening was designed for behavioral training and data recording. An adjustable shelf was made using a three-dimensional (3D) printer

and attached to the box right under the opening (Figure 2.2). The shelf carried a 3D force and torque transducer (Nano17, ATI Industrial Automation) that was positioned outside the window at about 1 cm distance. The rats were trained to reach and pull on a vertical metal bar that was attached to the transducer. An automatic food dispenser was attached to the box and dropped sugar pellets to a tray that was placed inside the box upon instruction. The output of the force transducer was continuously monitored and used to trigger the food dispenser.

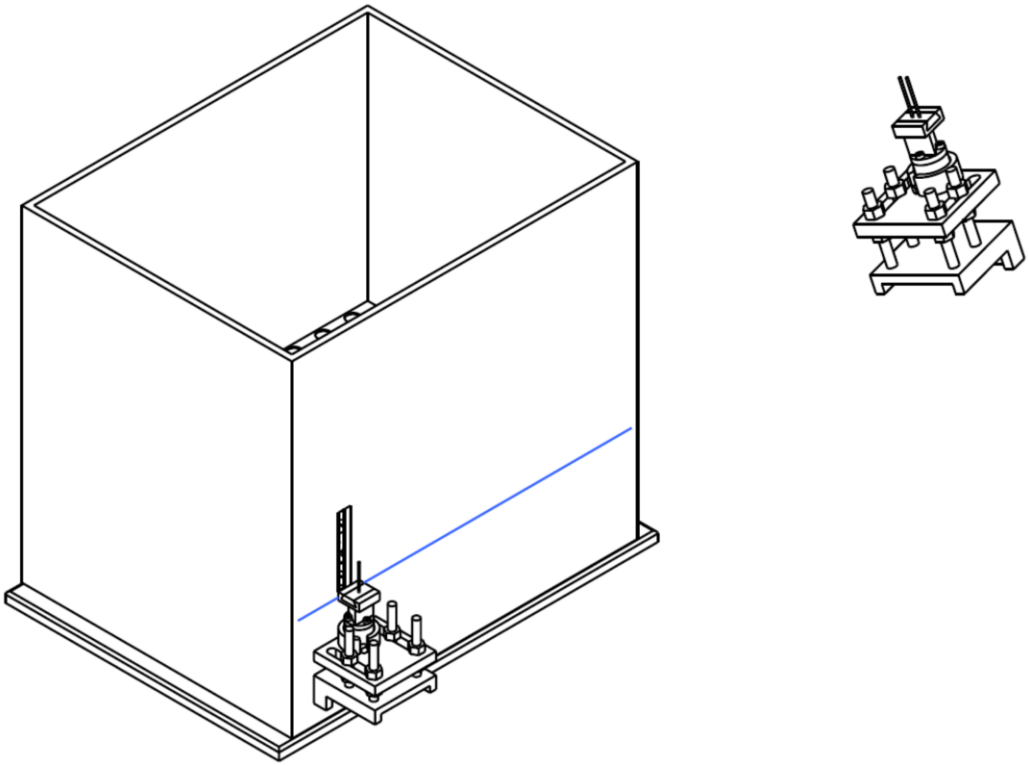

Figure 2.2 Plexi-glass box with the adjustable shelf attachment. The box had a vertical window (3x1 cm) for rats to reach through. A force transducer with a vertical metal bar was attached to the shelf. The output of the force transducer was continuously monitored, and the force level was used as a trigger to activate a food dispenser (not shown).

2.1.3 Animal Training

All procedures were approved by the Institutional Animal Care and Use Committee (IACUC), Rutgers University, Newark, NJ. Five Long Evans rats (350-450 gr) were used

in this study. Rats were placed in the training box and were trained to reach and pull on a vertical metal bar that was attached to the force transducer. Initially, a sugar pellet was placed right outside the window for the rat to retrieve using its tongue. The distance of the pellet was increased gradually until the rat began to extend its forearm to reach and retrieve the pellet. Each time the rat touched the bar (unintentional in the beginning) a sugar pellet was released from an automatic food dispenser as a reward. The rats were able to associate the bar pulling behavior with the reward within a day or two using this staging technique. The force threshold that triggers the food dispenser was gradually increased to maximize the recruitment of the forelimb muscles. Training took about one week, after which the rats were able to complete over 100 trials in a typical session. Figure 2.3 illustrates the behavioral task and the overall recording scheme.

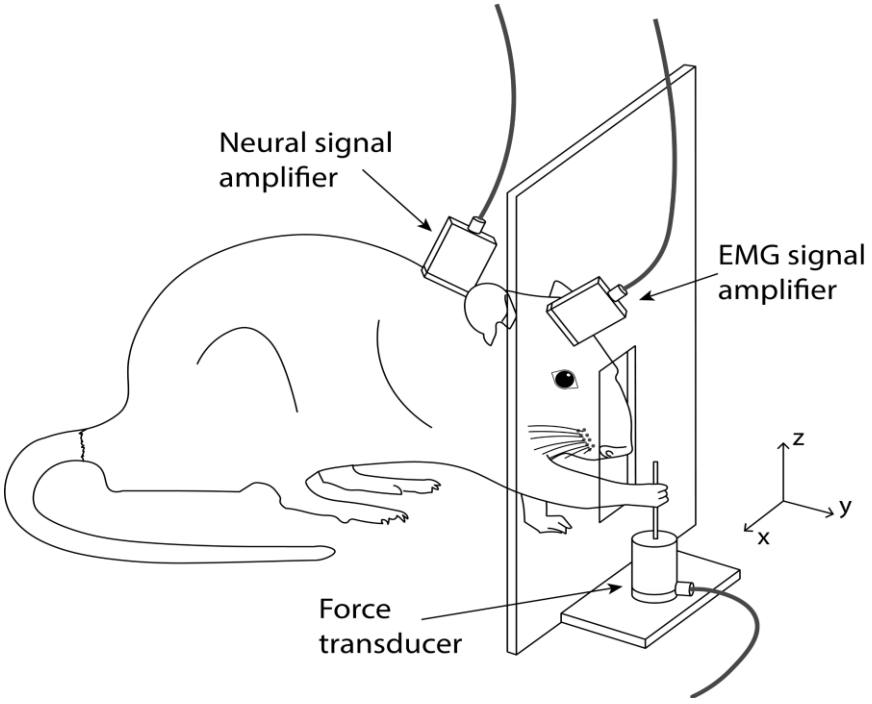

Figure 2.3 Reach-to-pull task. The neural and EMG signals were recorded simultaneously. The data was continuously buffered in a first-in-first-out fashion. Upon exceeding a pre-defined force threshold, neural, EMG and force signals within the last ±2 s with respect to time of the trigger were saved and two sugar pellets were dropped from a food dispenser as a reward.

Figure 2.4 demonstrates the components of a typical reach-to-pull task. Rat positions itself in front of the window and extends its elbow and wrist to reach the metal bar, followed by flexion of the elbow and the wrist to grasp and pull the bar. In the ideal scenario, rat's unused forelimb stays on the floor and rat uses only the forearm extensions and flexions to generate the pulling force.

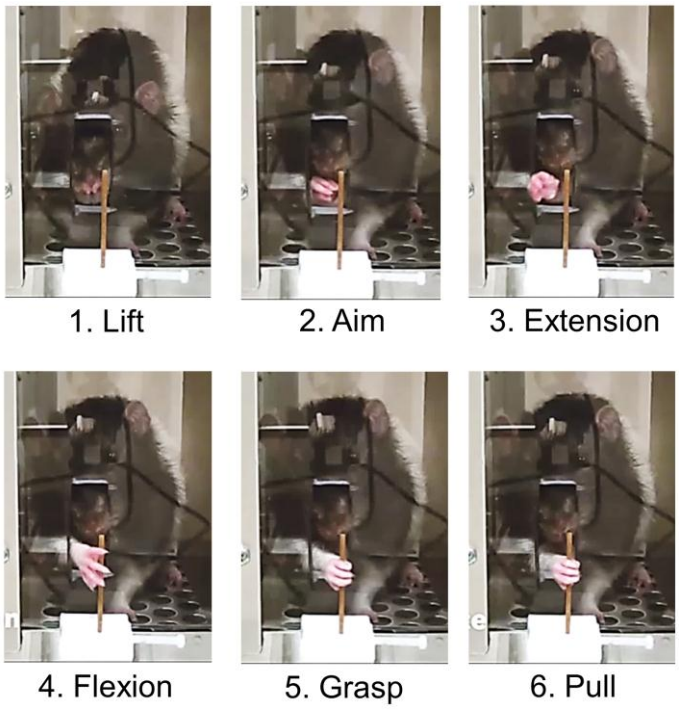

Figure 2.4 The components of a typical reach-to-pull task.

2.1.4 Electrode Implantation

The animal was placed in the induction chamber and vaporizer was adjusted to 4-5% isoflurane in 100% O2. Following the initial anesthesia, the rat was placed belly-down on a stereotaxic frame. The back of the animal's neck was shaved, and a skin incision was made along the midline. During surgery, the anesthesia was maintained by 2- 4% isoflurane gas inhalation. A heated plate (ATC1000, World Precision Instruments) was placed under

the animal to regulate the body temperature ~37°C. The heart rate and the blood oxygenation level were monitored with a pulse oximeter.

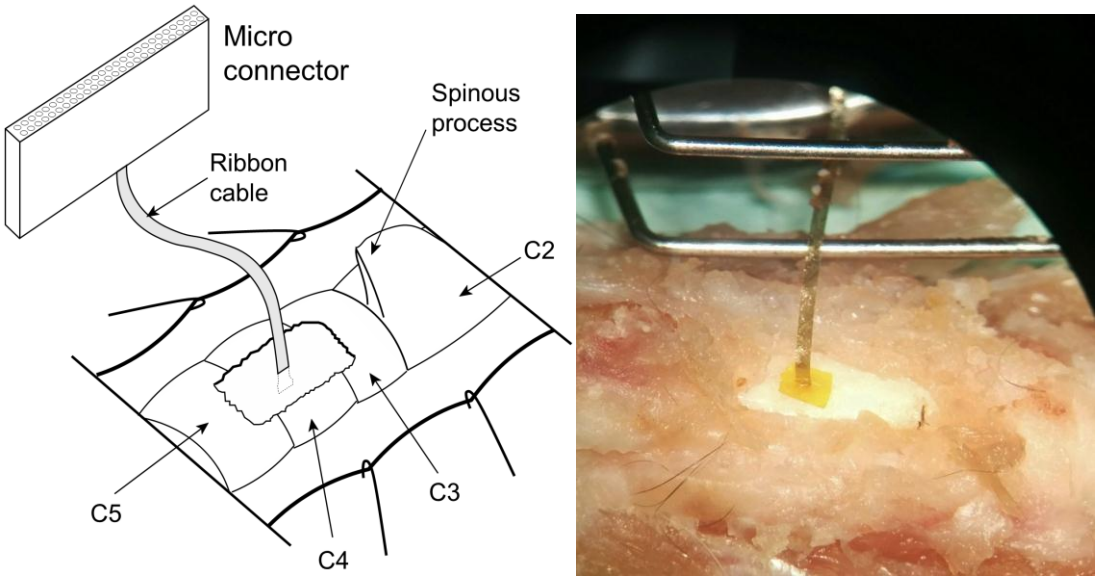

Figure 2.5 Electrode implantation into the spinal cord. Using a small rongeur, a hole was made on the dorsal C4 vertebra, while C3 and C5 were partially removed for easy access. The spinous process on the C2 vertebra was used as an anchoring point to hold the stainless-steel frame that carries the micro-connector. The frame is further secured by suturing it to vertebral bones of C5. The photo of an actual MEA implant is shown on the right. The orange colored Kapton© film was used as a stopper. The legs of the wireframe are also visible.

Following a dorsal laminectomy at C3-C4 levels, the custom designed planar electrode array (NeuroNexus, MI) was inserted down vertically for 1.3mm along the posterior median sulcus of the spinal cord into the CST, contacts facing the ipsilateral arm (Figure 2.5). The connector (Omnetics, MN) of the array was kept directly above the implant site protruding through the neck skin and anchored to a stainless-steel wire frame (with dental acrylic) that is attached to the 2nd and 5th vertebrae using silk sutures. The detailed picture of the electrode assembly with the wire frame can be seen in Figure 2.6. The ribbon cable was fixed to the pia mater using trace amounts of cyano acrylate glue and had a slack to avoid any pulling on the array.

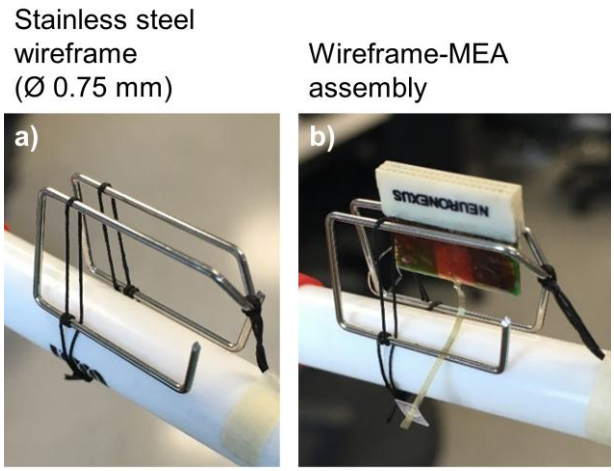

Figure 2.6 The wireframe was made from stainless steel wire with a diameter of 0.75 mm (a). The connector of the MEA was anchored to the wireframe (with dental acrylic) that was attached to the 2nd and 5th vertebrae using silk sutures (b). The white cylinder is a substitute for the spinal vertebral column in this picture.

EMG activities of four forelimb muscles (biceps, triceps, wrist extensors, and wrist flexors) were recorded using Teflon coated stainless steel wires (7 strands, 25 μm each, 793200, A-M Systems, WA). Four pairs of such wires (Figure 2.7) and a ground wire were attached to an Omnetics connector using electrically conductive epoxy (H20E, EpoTek, MA). Four small skin incisions were made to expose the targeted muscles in the upper and lower forearm. The EMG wires were tunneled subcutaneously using a hollow metal tube from the back of the head to the forearm incision sites. Electrode wire tips were staggered in pairs by ~4mm and sutured with 6-0 silk suture epimysially on the exposed muscles and further attached with cyano acrylate glue. The EMG micro-connector was then fixed to the skull using metal screws and dental acrylic. Animals received 0.05 ml buprenorphine (Buprenex® 0.3 mg/mL, diluted in saline) subcutaneously immediately after surgery and for 3 consecutive days thereafter.

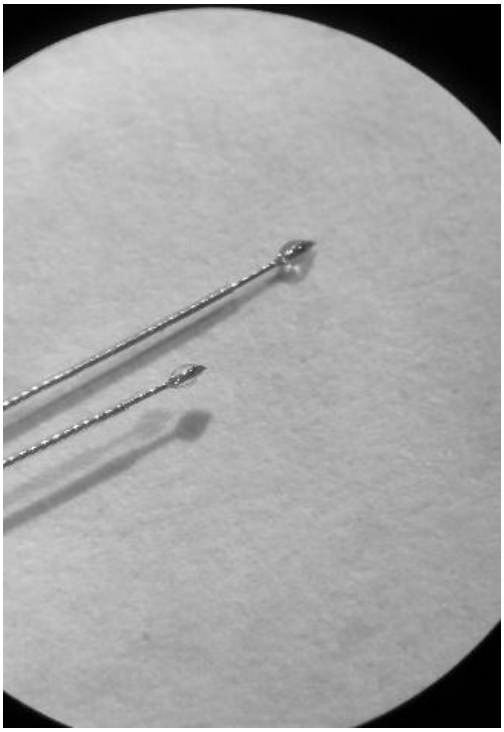

Figure 2.7 A pair of Teflon coated multi-strand 140 μm diameter stainless steel wire (25 μm strand diameter) were used as the EMG electrode. The wire tips were dipped into clear epoxy to form an encapsulation around the tip to prevent damage to the tissue and provide an anchor for suturing to the muscle.

2.1.5 Data Recording

Five rats were trained and implanted (R1-R5). After full recovery from surgery, animals were placed inside the plexi-glass box for recording. The force/torque sensor measured the 3D forces applied to the metal bar by the animal. The data acquisition system implemented a circular buffer to backlog all the data within 4 s window. The system automatically detected rat's pulling on the bar which was succeeded by activation of a food dispenser to deliver a sugar pellet.

Neural and EMG signals of R1 and R2 were amplified and transmitted by a 64-channel wireless amplifier (TBSI, NC) at 16kHz sampling frequency (Figure 2.8). For R3, R4, and R5 a tethered head-stage amplifier (Nano2 and Scout, Ripple, UT) with 30kHz

sampling rate was used (Figure 2.9). Episodes of neural, EMG, and force signals were recorded simultaneously during reach-to-pull and face grooming activities as well as in quiet and anesthetized states (Figure 2.10). Electrode impedance measurements were taken at 1 kHz using a multi-channel impedance meter (NiPOD, NeuroNexus, MI). The technical specifications of the recording systems are given in Table 2.1 and Table 2.2.

Figure 2.8 64-channel wireless recording system (Triangle BioSystems International).

Source: Wireless Recording Systems. http://www.trianglebiosystems.com/w-series-systems.html. Accessed March 20, 2018.

Table 2.1 Specifications of the TBSI Wireless Amplifier

Parameter	Typical	Units	Notes
Input voltage range	4	mV	Maximum input voltage Vpp
Gain selection	790-810		Factory selectable total system gain
Bandwidth	0.8-7000	Hz	-3dB input signal level BW
Input impedance	6.5	Mohm	At 1kHz
Input referred noise	8.5	µVrms	For DC 10kHz frequency, 30 µV
Input referred noise	5.5	µVrms	For 500Hz-5kHz frequency
Sampling rate/channel	50	kHz	At headstage (max 30kHz at ADC)

Source: Wireless Recording Systems. http://www.trianglebiosystems.com/w-series-systems.html. Accessed March 20, 2018.

Figure 2.9 Tethered front-end amplifier (RippleNeuro, UT).

Source: Recording Products. http://rippleneuro.com/front-ends?tab=recording. Accessed March 20, 2018.

Table 2.2 Specifications of the Nano2 Tethered Amplifier

Parameter	**Notes**
Resolution	16-bit - 0.125, 0.25, or 0.5 μV/bit (programmable)
Input range	± 4, 8, or 12 mV (set by resolution)
Sampling frequency	30 ksps
Hardware filtering	0.1 - 100 Hz HPF (programmable) 7.5 kHz LPF
Impedance measurement	10 k Ω to 1.0 MΩ electrodes
Input- referred noise	< 2.1 μVrms

Source: Recording Products. http://rippleneuro.com/front-ends?tab=recording. Accessed March 20, 2018.

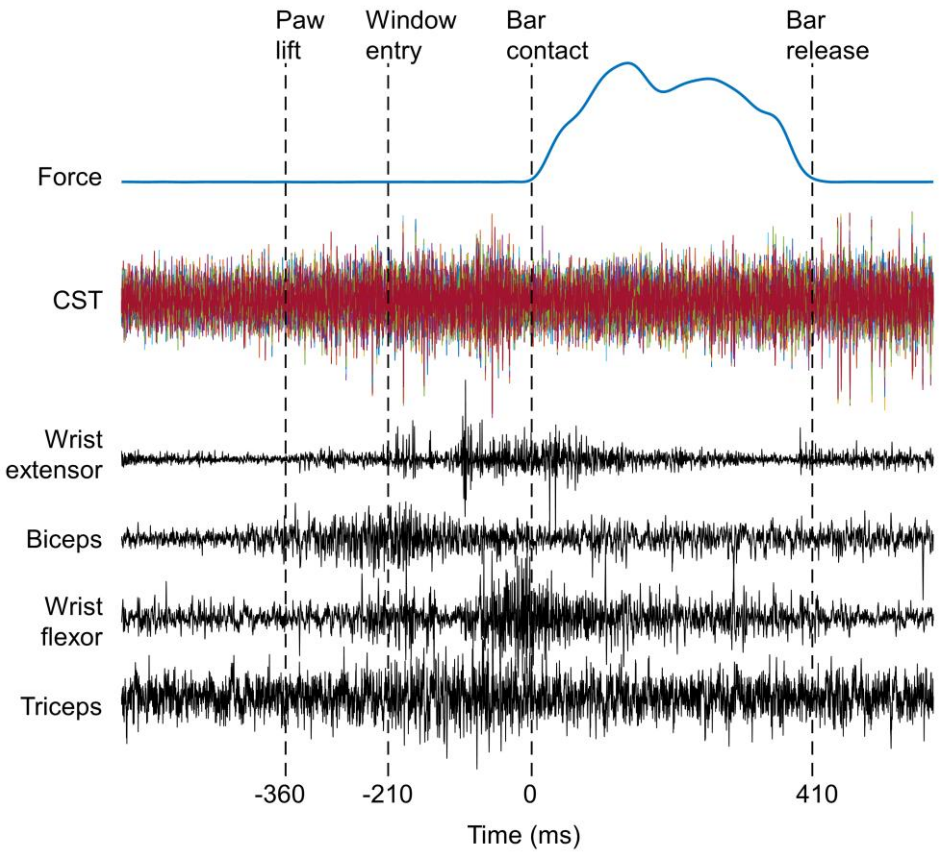

Figure 2.10 The force signal (blue trace), multi-channel CST recordings, and individual EMGs from four forelimb muscles, wrist extensors and flexors, biceps, and triceps (black traces) recorded during a typical reach-to-pull task. Vertical dash lines indicate phases of the forelimb movement in this trial.

Video images were also recorded at 30 fps to evaluate the quality and duration of the behavior. A trial refers to 3 or 4 s data collected during a behavior, while a session refers to all the trials collected from an animal on the same day. Multiple sessions were recorded in each animal before they are terminated. All recordings and subsequent data analysis were performed using custom scripts written in MATLAB (MathWorks, MA).

2.2 Data Analysis

2.2.1 Artifact Elimination and Channel Selection

The peak-to-peak amplitudes of the neural signals varied in a range of 50 μV to 150 μV over a background noise of ~10 μVrms. Signals with amplitudes exceeding ±200 μV and with durations longer than a typical action potential (>2ms) were considered as motion artifacts and channels containing such artifacts were excluded from further processing. Trials with fewer than 10 usable channels were also excluded from data analysis. The process of eliminating channels due to the presence of artifacts will be referred to as "data cleaning" in subsequent sections.

2.2.2 Long Term Signal Stability

In order to eliminate the CST signals not associated with the reach-to-pull task, only the 0.6 s of the data segment that captures the behavior was used (see Figure 2.10). First, the time of bar-touch was detected from the force profile and the neural data was cropped at 0.3 s before and 0.3 s after this time point (t=0). The CST signals were band-passed filtered between 80Hz – 3.5kHz and sifted through the data cleaning process described above. Two different metrics were used to assess the long-term signal stability. In the first method of stability assessment, the average inter-channel correlation coefficient (ICCC) across multiple trials was computed during the behavior and reported as a measure that reflects the degree of similarity among the recorded channels. In the second method, the root-mean-square (RMS) values of the differential signals that were obtained by subtracting the Common Average Reference (CAR) from each recording channel were calculated and averaged over all channels. Both methods were applied to all available trials within each session and means and standard deviations were reported for all five rats.

2.2.3 Average Inter-Channel Coherence

Magnitude-squared coherence estimates of neural signals were calculated for reach-to-pull (n=130), face-grooming (n=160), and quiet (n=130) trials on data segments with a duration of 1 s. Data segments for face-grooming and quiet trials were manually marked by examining the video and EMG recordings. For reach-to-pull task, data was marked at -0.7 s and 0.3 s with respect to bar touch, in order to capture the entire behavior. The CST signals underwent data cleaning procedure and 20 qualified channels that were common to all trials were retained. Coherence analysis (100 ms window length, Hamming window, 50% overlap) was applied to all pair-wise contact combinations, an average inter-channel coherence vector was obtained for each trial, and then averaged across all trials and plotted along with 95% confidence intervals.

2.2.4 Average EMGs

Reach-to-pull task involves flexion and extension of the wrist and the elbow. Components of the reach-to-pull task can be determined by examining the muscle activation patterns of biceps, triceps, wrist extensors, and wrist flexors. However, rats demonstrated various behavioral patterns during trials, such as multiple reaches, resting paw on the force plate, and weak pull attempts prior to the final and strong one. Nevertheless, the rats exerted similar forces if they followed a movement trajectory that involved consecutive paw-lift, reaching, and single pulling. By examining the force data, we were able to group the trials with similar average muscle activation patterns. RMS power extracted from 1 s of force data preceding the bar touch, was used as a metric to distinguish between reproducible forelimb movements and the outliers (Figure 2.11A). Reproducible movements with no prior activity before pulling had low RMS values reflecting the baseline force signal

whereas others (multiple touches or paw resting on force plate) had large RMS values, sign of deviation from the baseline force. Using simple thresholding on these RMS values, the outliers were detected and excluded from analysis.

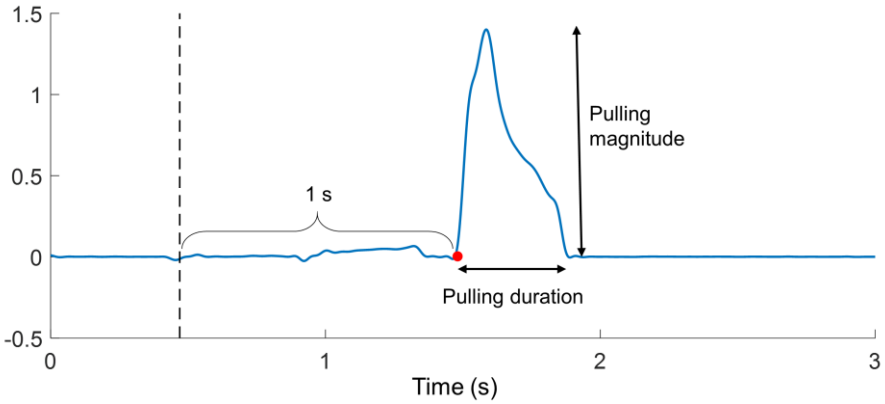

(a)

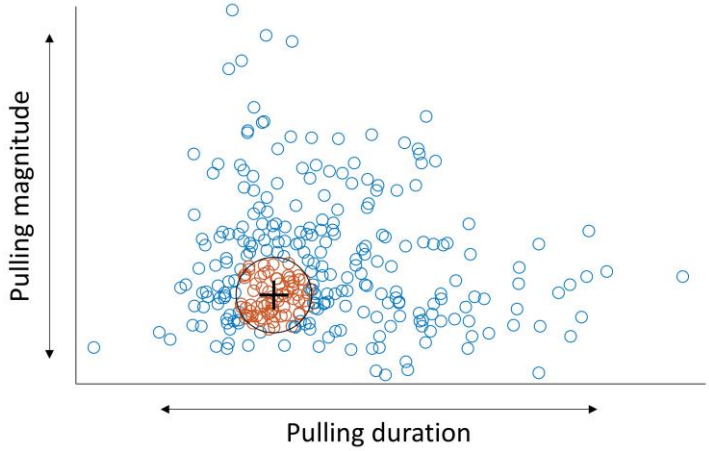

(b)

Figure 2.11 a) The procedure of identifying trials with reproducible forearm movements to be used in EMG averaging. Red dot indicates the moment of bar touch. RMS value of 1 s of force data preceding the bar touch was used as a metric to distinguish between reproducible forelimb movements and the outliers. Pulling magnitude and duration were used to further improve the similarity criteria. b) Scatter plot of the trials that passed the outlier removal stage. All trials that fell inside a circle that was centered at the feature medians with a radius of $\frac{1}{2}iqr_{min}$ were kept (red circles) while all others (blue circles) were discarded. The average EMGs were computed using the retained trials.

In the next step, the pulling force amplitude and the pulling duration were obtained from the remaining trials to create a two-dimensional feature set. The inter-quartile-range

(iqr) was computed in both dimensions and half of the smaller iqr was found (½iqrmin). All trials that fell inside a circle with a center at the feature medians and a radius of ½iqrmin were kept while all others were discarded (Figure 2.11B). Once the final group trials were identified, the EMG signals were band-pass filtered between 80Hz – 2kHz, normalized by their respective standard deviations, rectified, and finally, low-pass filtered at 20Hz to obtain the EMG envelopes. The average EMG envelopes were plotted along with the 95% confidence intervals. The information gained by examining the average EMG profiles will be used to identify the phases of forelimb movement in the classification stage.

2.2.5 Classification

Based on the results of the coherence analysis, two distinct bands were identified in the frequency spectrum of the CST signals associated with the forelimb movements; the lower-frequencies (LF) associated with high coherence values spanning from 200 to 1500 Hz, and the upper-frequencies (UF) that had lower coherence values spanning from 1500 to 3500 Hz (see Figure 3.4). Classification, a supervised machine learning technique, was employed to build a predictive model in which the CST signals were the predictors and the forelimb movement phases (reaching, pulling, etc.) were the classes. To extract the features from the CST signals of a desired movement phase, the time-frequency spectrogram of each CST channel was computed using the short-term Fourier transform (STFT) with a 100 ms moving window (Hanning) advanced in 10 ms steps. The resulting spectrogram was divided into 4 segments for 2-class (Figure 2.12) and 6 segments for 3-class classification separating LF-UF bands and movement phases, and each segment was summed along both time and frequency, generating one value per segment.

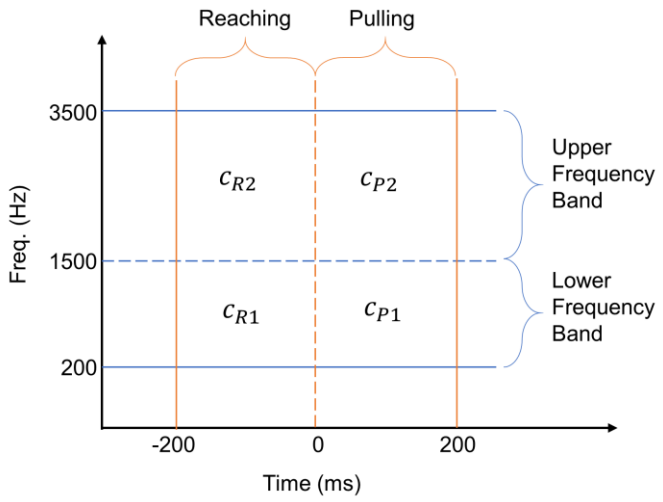

Figure 2.12 Identification of the features (total energy in the LF and UF bands) with respect to movement phases (reaching vs pulling) of a single channel for the 2-class classification scheme. We followed the same reasoning for the 3-class classification problem (not shown).

When all 27 channels were used, the final feature vector included a total of 54 coefficients, 27 from LF and 27 from UF. Each LF and UF sub-vectors were normalized by subtracting the mean and dividing by the standard deviation, so that classification would not be biased toward magnitude shifts between feature vectors. Instead, the classification algorithm looked for the differences between the corresponding channels or patterns in the channel coefficients, which would indicate a spatially distributed information in the CST signals. Details of the movement phases and classification inputs can be seen in Table 2.3 for a session of N=100 trials. The force signal generated in the horizontal plane towards the rat was used to detect the onset and offset of the pulling behavior. In the 2-class classification scenario, the above procedure was applied to the CST data within the 200 ms window preceding the pulling onset and labeled as “reaching” and repeated for the 200 ms window succeeding the pulling onset and labeled as “pulling”. As for the 3-class classification, three 100 ms windows were identified by examining the average EMG

signals (Figure 3.6). Each window underwent the same feature extraction procedure and labeled as “wrist extension”, “wrist flexion”, and “grasp”, consecutively (Table 2.3).

Table 2.3 Time Intervals (With Respect to Bar Touch) of Movement Phases for 2-class and 3-class Classification Paradigms

	2-class		**3-class**		
Phase	Reaching	Pulling	Extension	Flexion	Grasp
Phase interval (ms)	[-200 0]	[0 200]	[-200 -100]	[-100 0]	[0 100]
# of features (e.g. 27 channels)	54	54	54	54	54
# of observations (e.g. 100 trials)	100	100	100	100	100
	Total: 200		Total: 300		

Once the features were extracted, the input matrix was formed and forwarded to the classification stage. In this stage, multiple classification algorithms were tested, and their performances were compared. To avoid overfitting and increase the generalizability, the classification algorithm selected a smaller subset of features using either sequential feature selection (SFS) method or predictor importance (PI) metric. In the SFS technique, the features are added sequentially until addition of a new feature did not lead to any improvement in the classification performance in the training set. The PI metric on the other hand was used to sort the features according to their importance, and only a selected set of the most important features were used in the classification. To estimate the classifier performance, which was defined as the percentage of the correct predictions, 5-fold cross-validation technique was used. Since the accuracies were observed to change between classification attempts due to randomized initial weights, classifiers were run 11 times and

the average accuracy was taken. Details of the classification techniques are given in Table 2.4. Figure 2.13 illustrates the flow chart of the classification analysis.

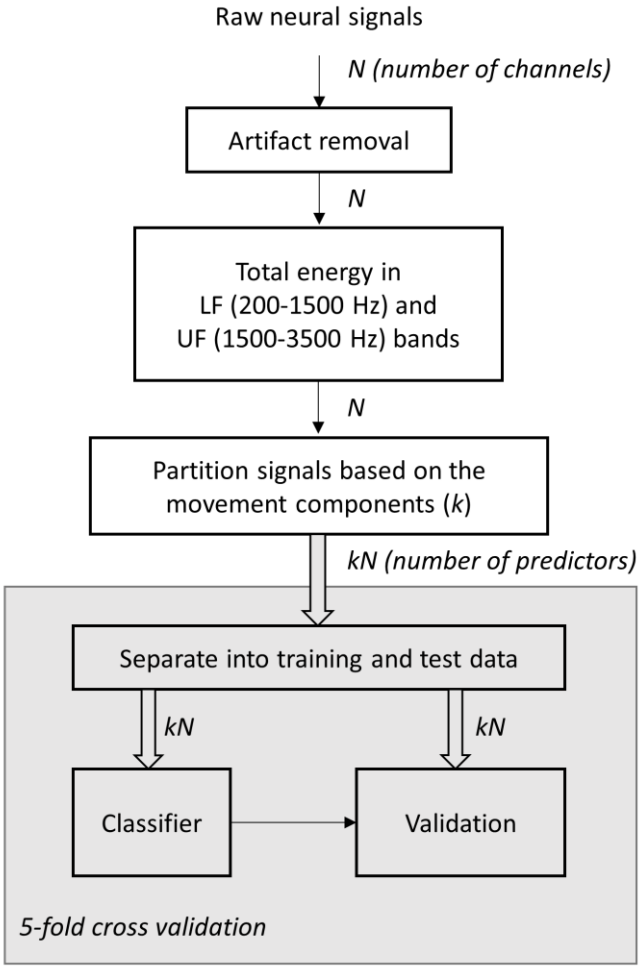

Figure 2.13 Flow chart of the classification analysis used to segregate movement components. Both 2-class and 3-class scenarios used the same scheme with different number of component (*k*).

Table 2.4 Algorithms used for classification. SFS: Sequential Feature Selection, PI: Predictor Importance

Classifier	Feature Selection	Description
Linear Discriminant Analysis (LDA)	SFS	—
Support Vector Machines (SVM)	SFS	—
Naïve Bayes (NB)	SFS	With linear kernel function
k-Nearest Neighbor (KNN)	SFS	*k* optimized by cross-validating training set
Random Forest (RF)	PI	200 trees used

2.2.6 Linear Regression

Linear Regression analysis was performed on CST signal envelopes to predict the EMG envelopes for trials recorded during reach-to-pull tasks. The force signal generated in the horizontal plane towards the rat was used to detect the onset and offset of the pulling behavior. The data segment starting at 0.5 s before the pulling onset and ending at the pulling offset was clipped for processing. Data segments had varying lengths depending on the pulling duration, with the average length being ~1 s. Following the data cleaning and clipping step, all available trials in a particular session were concatenated, and treated as a single continuous trial. As in the classification analysis, the CST signals were divided into two parts by band-pass filtering between 200-1500 Hz (LF) and 1500-3500 Hz (UF), respectively. This generated a dataset with 2*N features for a trial with N usable channels, on which Principal Component Analysis (PCA) was performed. The EMG signals were band-pass filtered between 80-2000 Hz and both EMG channels and principal components (PCs) were rectified and low-pass filtered at 4 Hz. The PCs were further sorted in descending order of variance and normalized before the regression stage.

Backward elimination technique was used to find the optimal set of regression coefficients without overfitting. In this technique, a predictive model was initialized using all the features in the training set; the prediction was made on the test set containing the same features; and the mean-squared error (MSE) was calculated using the actual and predicted signals. In the following steps, the features were eliminated sequentially until the removal of additional features does not decrease the MSE. The remaining features were used to build the final model. The prediction performance was reported as the correlation coefficient (CC) and coefficient of determination (R^2) between the actual and predicted signals. A 5-fold cross-validation technique was employed to assess the overall prediction performance (average of all fold predictions). Regression analysis performed on each EMG channel separately. The flow chart of the regression analysis is given in Figure 2.14.

$2N$ features (LF and UF vectors) from N channels were extracted, and the prediction algorithm transformed these features, first by multiplying with a transformation matrix (PCA), and second by multiplying with regression coefficients (prediction). PCA produces a coefficient matrix that was used to construct the principal components and regression produces a coefficient vector as the model parameters. By tracing prediction steps backward, i.e. taking the inverse of coefficient matrix, one can determine the contributions made by individual input channels to form the final output. However, using only the PCA and prediction coefficients would be misleading because a large coefficient alone does not exclusively determine contribution without considering the neural signal amplitudes. We calculated the weight of a particular feature in a certain PC by multiplying that channel by its corresponding coefficient and finding the RMS value of the product. We repeated this for all features and all PCs, and formed a weight matrix, called *A*.

Following the same procedure for the regression step, we calculated the weight of a selected PC by finding the RMS value of the product of the PC and its regression coefficient. Repeating this procedure for all PCs, we generated a weight vector, called *B*. By multiplying vectors *A* and *B*, we derived the vector *C* that included the contributions made by individual features, such that:

$$\begin{matrix} \mathbf{A} & & \mathbf{B} & \mathbf{C} \end{matrix}$$

$$\begin{bmatrix} a_{11} & \cdots & a_{1m} \\ \vdots & \ddots & \vdots \\ a_{m1} & \cdots & a_{mm} \end{bmatrix} \times \begin{bmatrix} b_1 \\ \vdots \\ b_m \end{bmatrix} = \begin{bmatrix} c_1 \\ \vdots \\ c_m \end{bmatrix} \tag{2.1}$$

where a_{ij} is the weight of feature i in PC j, b_i is the weight of PC i in predicted signal, c_i is the contribution made by feature i to the predicted signal, and m is the number of features that were used in the prediction algorithm. Once we obtained the contributions of the features, we computed the overall contribution of a channel and a frequency band (LF vs UF) by using simple arithmetic, such that:

$$c_{LF} = c_1 + c_2 + \cdots + c_n \tag{2.2}$$

$$c_{UF} = c_{n+1} + c_{n+2} + \cdots + c_{2n} \tag{2.3}$$

$$c_{CHi} = c_i + c_{n+i} \tag{2.4}$$

where c_{LF} is the contribution made by the features that represents the lower frequency band, c_{UF} is the contribution made by the features that represents the upper frequency band, c_{CHi} is the contribution of $channel\ i$, and n is the number of channels. (Note that $m = 2n$.)

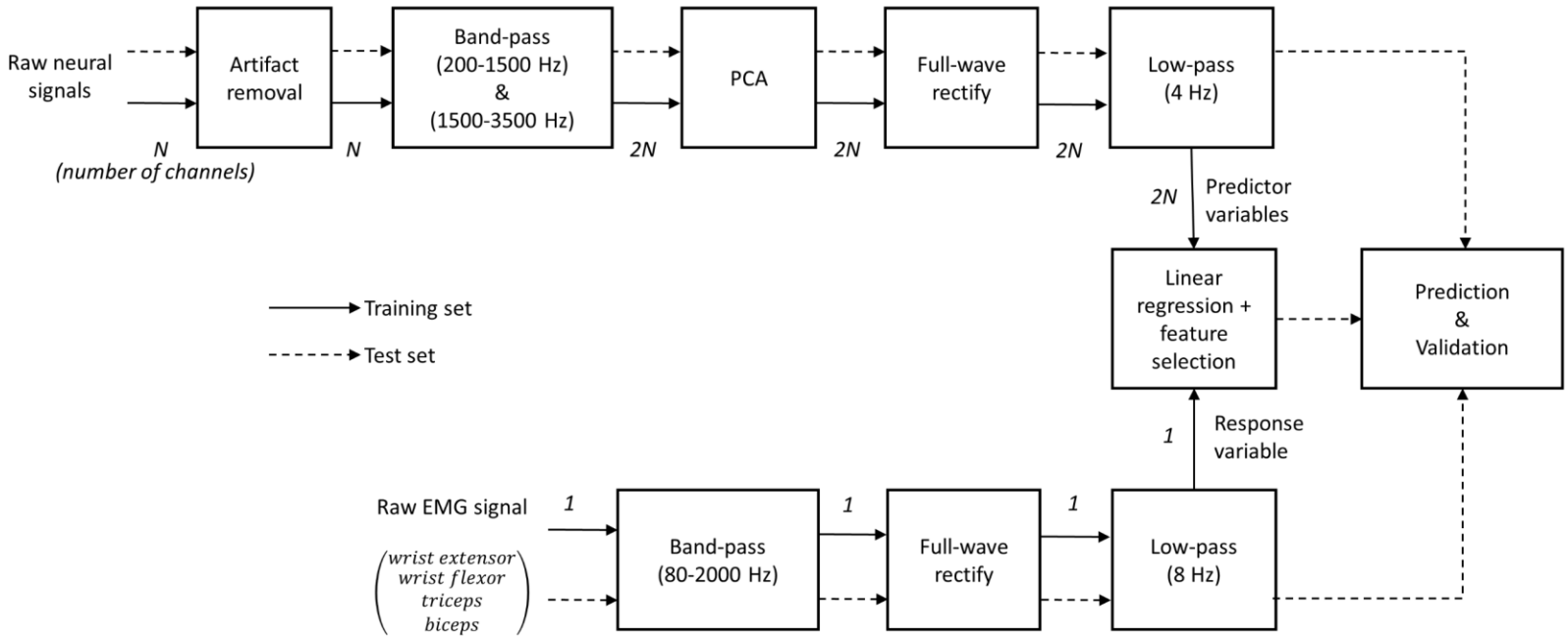

Figure 2.14 The flow chart of the regression analysis.

2.2.7 Confirmation of the Electrode Positions

The location of the multi-electrode array in the spinal cord dorsal column was confirmed with histology after termination. The implanted region of the spinal cord tissue was dissected out and sectioned for histological analysis. The sections were stained and examined under the microscope. The EMG electrode locations were confirmed to be in the vicinity of the targeted muscles by electrical stimulation (10 mA, 2 ms, and biphasic pulses at 50 Hz).

2.2.8 Immunohistology

At the end of the experiments, animals were anesthetized by administering a ketamine-xylazine cocktail and perfused using 4% paraformaldehyde (PFA) solution. The implanted region of the spinal cord tissue was dissected out and stored in 4% paraformaldehyde to obtain frozen sections. 15 micron thick sections were stained with Luxol Fast Blue (LFB, myelin marker) and Haemotoxylin and Eosin (H&E) to assess the demyelination and the extent of the tissue response due to the MEA. The stained sections were analyzed by light microscopy.

Luxol Fast Blue (LFB) Staining: Luxol fast blue (LFB) is used to stain myelin and myelinated axons on formalin-fixed and frozen or paraffin embedded neural tissue sections. LFB is mainly used to detect demyelination in the central nervous system. Under LFB stain, myelin sheets appear light blue, neuropil appears pink, and nuclei appear purple. LFB can distinguish between spinal cord white matter and gray matter.

Haemotoxylin and Eosin (H&E) Staning: H&E is the standard staining procedure in histology and widely used as the first approach to inspect the tissue samples. H&E stains the nucleus and the cytoplasm with two different dyes, thus making the cells visible for

morphological examination. In H&E, the cytoplasm and the extracellular matrix are stained in varying shades of pink, and the nuclei are stained in dark blue or purple. H&E can also distinguish between spinal cord white matter and gray matter.

CHAPTER 3

RESULTS

3.1 Neural Signal Processing

3.1.1 Signal Power

Figure 3.1 shows the power spectral densities (PSD) of the measured neural activities during various behavioral states. PSD values were calculated by performing Welch averaged periodogram method in MATLAB (MathWorks) on 0.5 s long data segments (average of 27 channels from 33 trials per behavioral state). The frequency range below 200 Hz exhibits significant power. This result was consistent with those of our previous studies in which different types of electrodes were used (Prasad & Sahin 2010; Prasad & Sahin 2011).

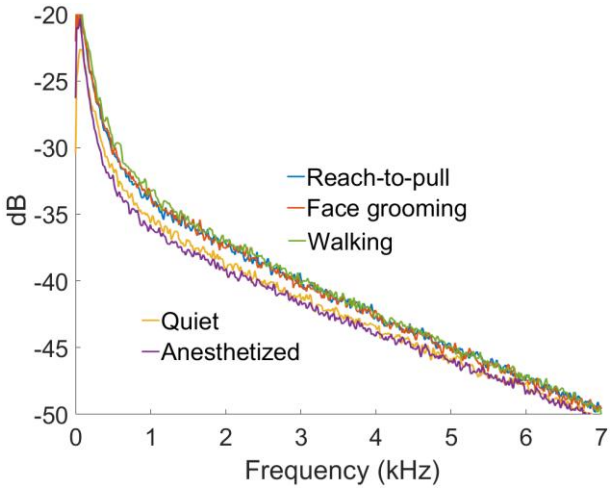

Figure 3.1 PSD of neural activity from CST. Upper three traces: reach-to-pull task, face grooming, and walking activities. Lower two traces: quiet and anesthetized states. PSD of 500 ms long data segments were averaged over 27 channels from N=33 trials per group.

Top three traces in the figure show the activities in which rat depends on its forearm. Reach-to-pull task requires the activation of shoulder, elbow and hand muscles, including

biceps, triceps, and wrist extensors and flexors (Hyland & Jordan 1997). For the face grooming and walking activities, a similar set of muscles are included in the behavior. The power level in the multiunit activity range (from 200 Hz to a few kHz) remained higher than those in quiet and anesthetized animal, suggesting an increased CST activity during forearm movement.

3.1.2 Impedance Measurements

The average contact impedances (N=13 for R1 and R2, N=27 for R3, R4, and R5) as a function of implant time are shown in Figure 3.2. R1 and R2 were both implanted with PEDOT:TFB coated Pt (Gok et al. 2015) arrays while the rest of the animals were implanted with uncoated Pt electrode arrays. Despite the fact that the coated contacts had significantly lower impedances, we did not observe distinct differences in the quality of the recorded signals. The average impedances increased about two weeks after implantation and then settled at a lower value around 1-2 MΩ, which is a trend typically seen in microelectrode implants in neural tissue (Figure 3.2).

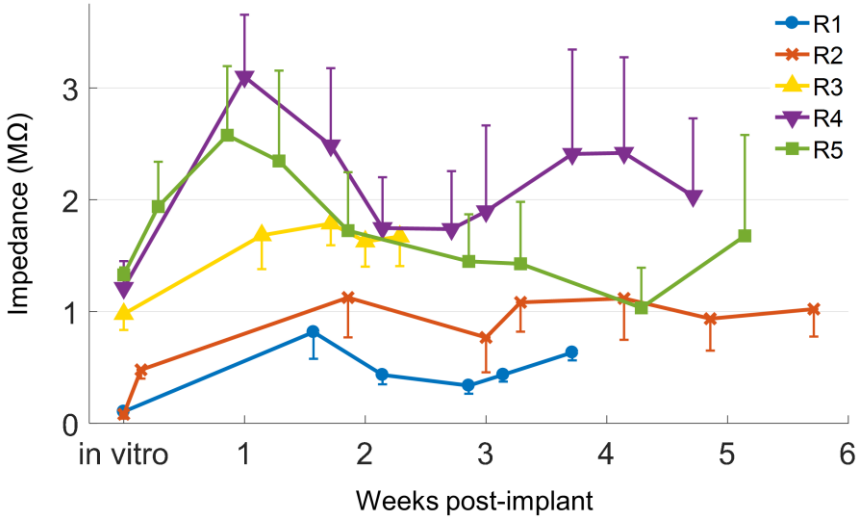

Figure 3.2 Average impedance measurements as a function of implant time. R1 and R2 were implanted with PEDOT:TFB coated Pt contact MEAs, while R3, R4, and R5 had plain Pt contacts.

3.1.3 Signal Stability

Figure 3.3 depicts the average inter-channel correlation and average channel-CAR difference measures as a function of implant time. The neural channels in R1 and R2 share a powerful common-mode signal as indicated by high correlations. In the remaining rats, however, the inter-channel correlations are much lower. The neural signals in R1 and R2 were recorded using a wireless amplifier where the large contacts on the array were shorted and used as a reference and no ground connection was needed. On the other hand, recordings of rats R3, R4, and R5 were performed using a tethered amplifier with separate ground and reference inputs. We believe that the difference in the level of common-mode signals between the two groups was due to the two different amplifiers with different referencing techniques. However, the common-mode signal was not necessarily an unwanted component, such as muscle EMG. The common-mode signals had to be of neuronal origin from the spinal cord since the recordings were made differentially in both groups with reference electrodes very near the contacts and the nearest muscles were relatively at a much farther distance. There is however still the possibility that in the first two rats, the origin of the common-mode signals might be the spinal gray matter near the recording array. The CAR signal was not subtracted in the classification and prediction algorithms. All rats exhibited a similar trend by the average signal amplitudes after the common-mode signal was subtracted out (bottom Figure 3.3). Finally, in the top panel of the Figure 3.3, the average ICCC of all rats fairly remained stable throughout the experiment, although R3 and R5 showed an increase around 3rd week which then returned to previous levels.

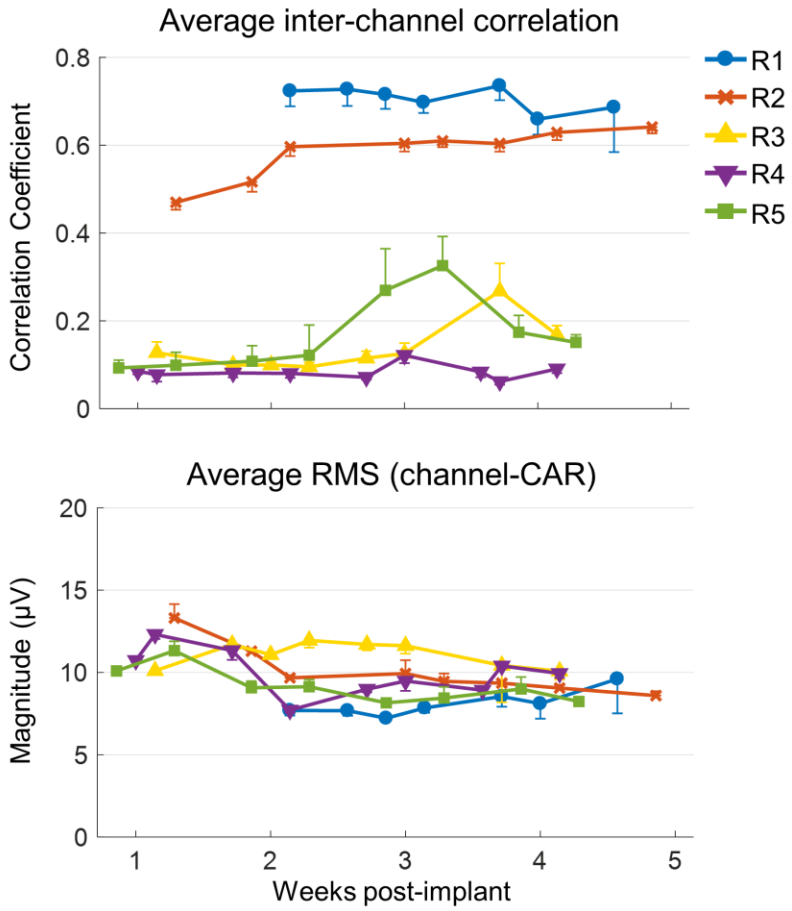

Figure 3.3 Average ICCC (top) and average RMS value of the channel – CAR (bottom) as a measure of implant time. Average ICCC of all rats fairly remained stable throughout the experiment, although R3 and R5 showed an increase around 3rd week which then returned to previous levels. All rats exhibited a similar trend in the average RMS power when the common mode was extracted from the neural signals.

3.1.4 Average Inter-Channel Coherence

Figure 3.4 compares the average inter-channel coherences for reach-to-pull task, face grooming behavior, and the quiet state. The coherence spectra contain an elevated band between 1 and 4 kHz that contains more power in reach-to-pull task and face grooming behavior, indicating the presence of multi-unit signals when the rat is active. Furthermore, a high coherence band below 1.5 kHz can clearly be seen in reach-to-pull task, whereas it is absent in the face grooming behavior and the quiet state. This suggests that the CST

signals that were responsible for voluntary forelimb movements manifested an increased activity below 1.5 kHz in addition to the 1-4 kHz band. Coherence plot in Figure 3.4 was also used to determine the lower and upper frequency bands that were introduced in the methods section. All behavioral states exhibited a steep rise below 200 Hz in the coherence spectra possibly due to the movement artifacts and their harmonics. Thus, frequencies below 200 Hz and above 3.5 kHz were not included in the classification and the regression analyses.

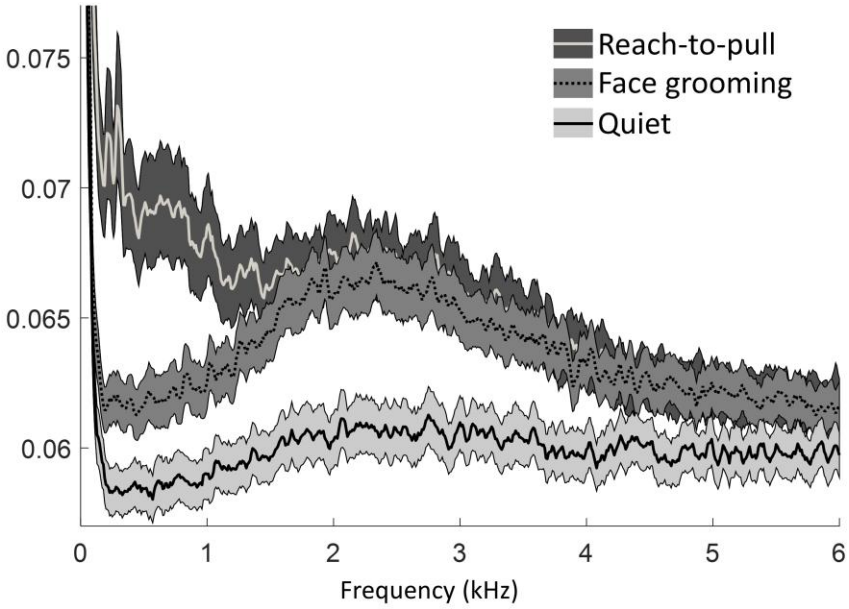

Figure 3.4 Comparison of the average inter-channel coherences for reach-to-pull task, face grooming behavior, and the quite state averaged over n=130, n=160 and n=130 trials from R3, respectively. Traces show average coherence vectors and shaded areas indicate 95% confidence intervals.

3.1.5 Average EMGs

Figure 3.5 shows the force profiles of the reproducible movements with no prior activity before pulling, which were obtained by the selection technique explained in the *Methods* section. The forelimb EMG envelopes followed typical trends as expected during the reach-to-pull task. The activity of the wrist extensors started to increase ~200 ms prior to pulling

onset indicating paw opening during forelimb reaching. The decline of extensor activity coincided with an increase in the activity of wrist flexors, which started around ~100 ms prior to pulling onset as an indication of paw closing. The biceps and triceps activation patterns support our observations that the reaching movement was started about 300-400 ms before the bar touch. During the pulling, all muscles were co-activated at different levels, extensors and biceps being the most prominent. By examining these muscle activation patters, we determined the movement components that will be used in the classification analysis. For 2-class classification, two windows were identified to represent the reaching and the pulling movements as depicted by light blue and tan colored backgrounds in Figure 3.6, respectively. For 3-class classification problem, three smaller windows were chosen as representatives of wrist extension and flexion, and bar grasping movements. These time windows are marked by solid red lines in Figure 3.6.

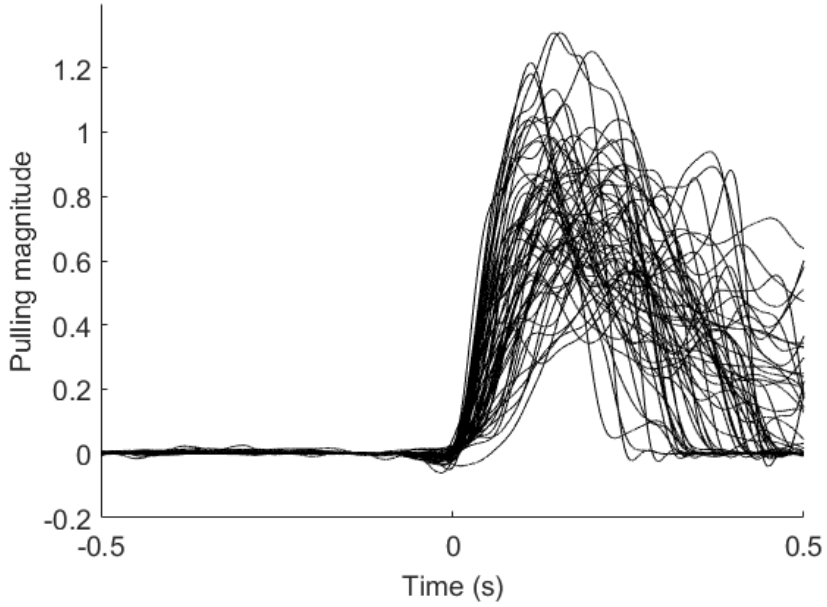

Figure 3.5 The force profiles of the selected reproducible trials that were used to find EMG averages.

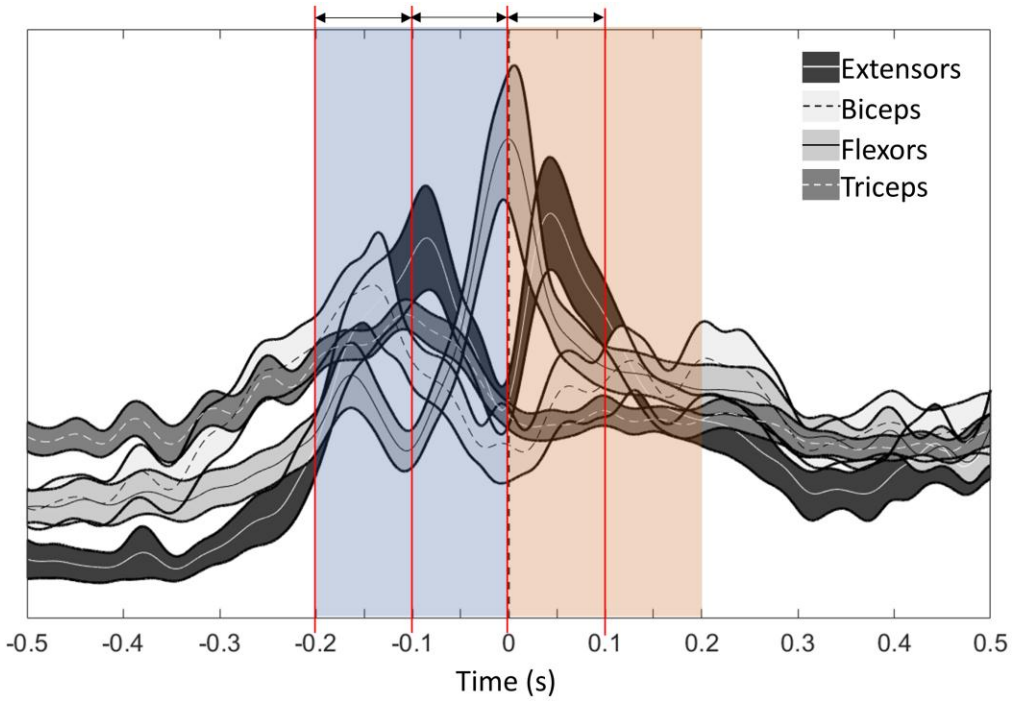

Figure 3.6 Average EMG profiles of forelimb muscles during reach-to-pull task. Light blue background indicates the "reaching" phase and tan background indicates the "pulling" phase. Wrist "extension", "flexion" and "grasp" phases are demarcated by vertical red lines and the arrows.

3.2 Modelling the CST – Forelimb Relationship

3.2.1 Movement Classification

The classification algorithm detected the patterns in the feature vectors as represented in Figure 3.7. Figure contains the means and standard errors (SE) of the feature values, a bar graph of estimates of feature importance, and distributions of mean feature values based on the actual channel positions (R1, session #5, N = 93 trials). In this particular example, the classification was performed using an *ensemble of bagged decision trees* (a.k.a. random forest) to obtain the estimates of predictor (feature) importance (MATLAB 2017b). This method calculates how much the features improve the split criterion, i.e., the variable that decision tree aims to maximize while deciding to choose features to put on each node of

the tree. The more the feature improves the criterion the more importance it is given. Figure 3.8 contains the same information for the 3-class scenario.

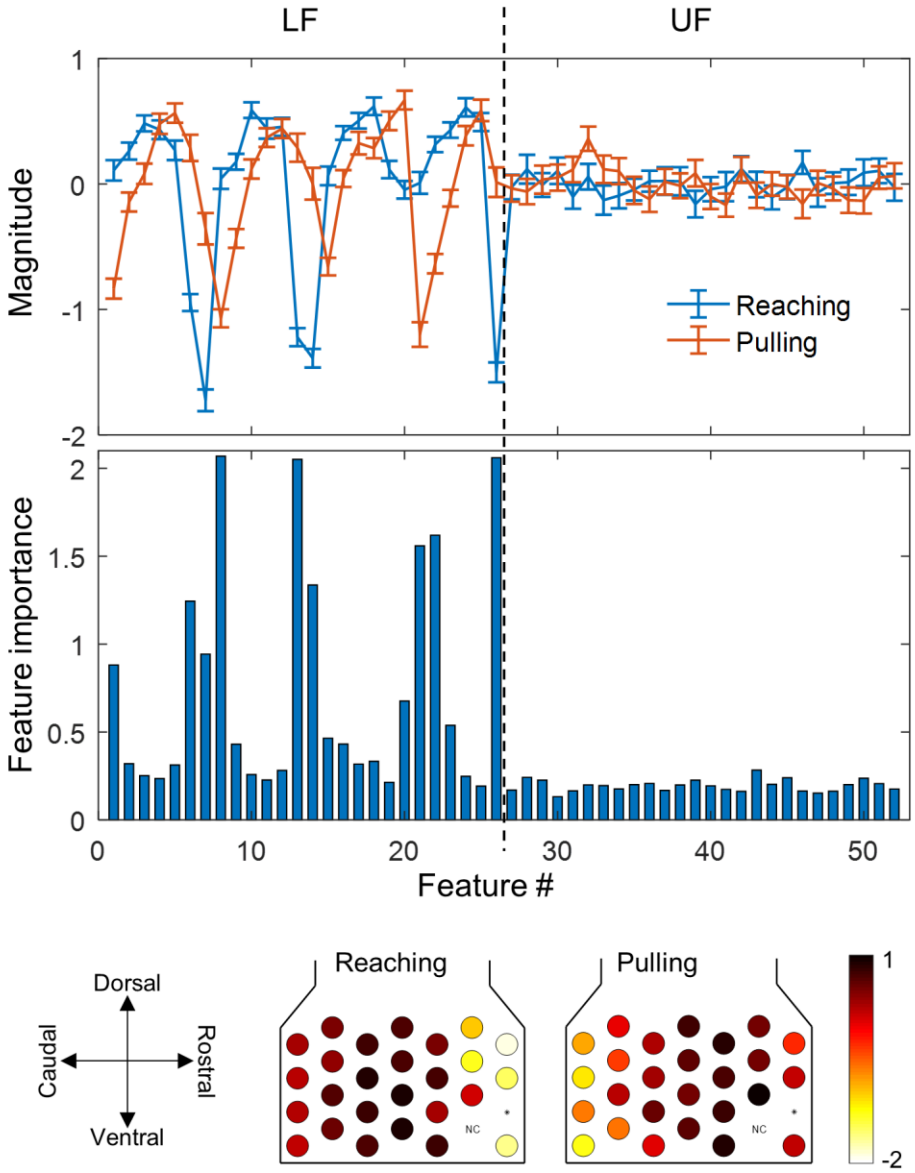

Figure 3.7 Patterns in the feature vectors for the 2-class scenario. Top panel: Average feature values (bars indicate standard errors (SE)). Middle panel: Feature importance assigned by the classification algorithm. Bottom panel: Spatially distributed mean feature values based on the actual electrode contact positions.

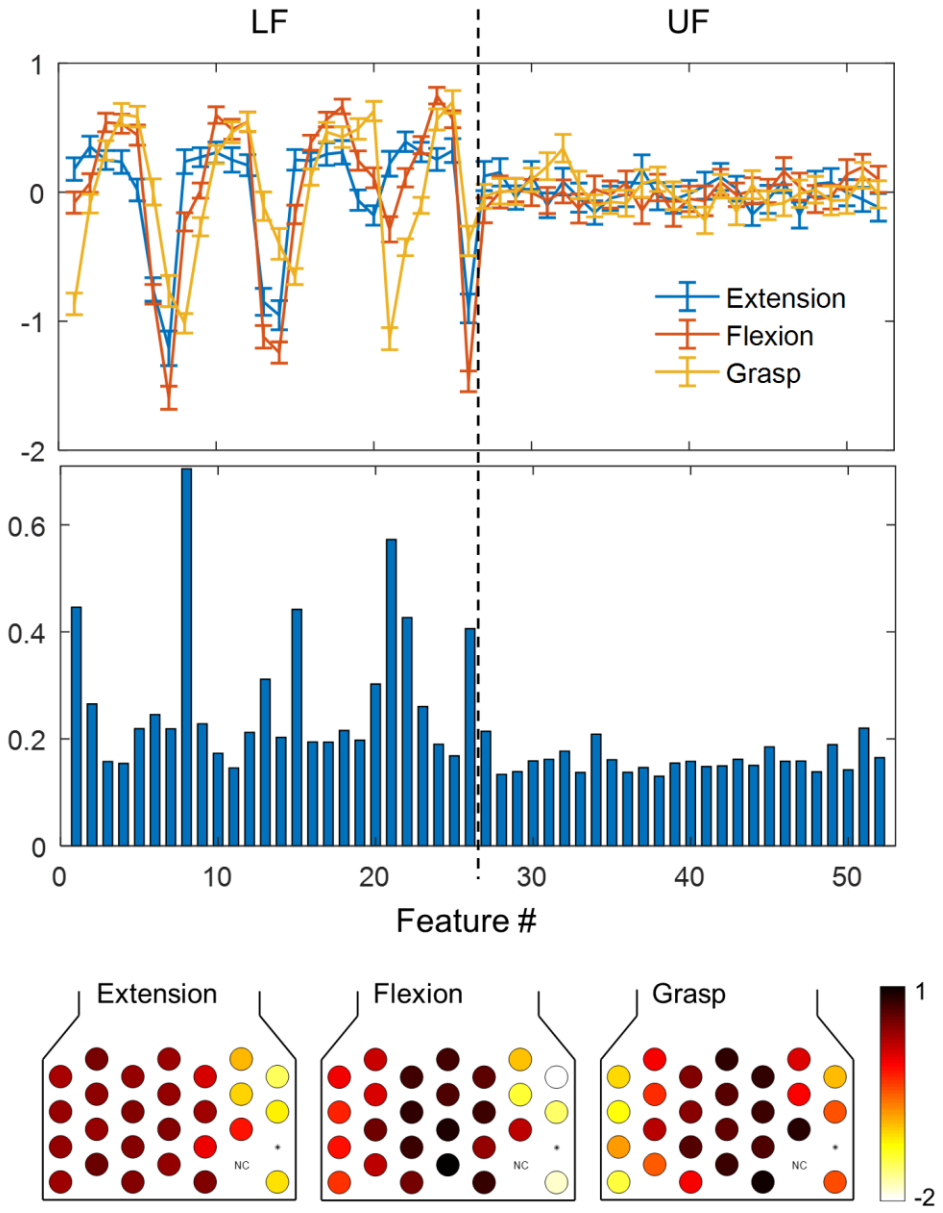

Figure 3.8 Patterns in the feature vectors for the 3-class scenario.

The features that differed substantially between movement phases (large distances between means and small SEs) were the primary contributors to the classification. Interestingly, the first half of the feature vector, which corresponds to the total energy in the LF spectrum (200-1500 Hz), was the major contributor, whereas the UF spectrum (1500-3500 Hz) had little or no effect in the classification. This was true for almost all

sessions and rats except a handful of sessions where features in the UF band also exhibited high importance metrics. Another important observation for this particular example was that the features were spatially distributed according to the movement phases, e.g. reaching vs. pulling in 2-class paradigm as shown in the bottom left panel in the figure. The heat maps are derived directly from the mean feature values (LF band only) given in the top panel. The contacts of the MEA is facing right the CST fibers ipsilateral to the preferred forelimb; i.e. the right edge of the array is more rostral than the left edge. During reaching, the contacts on the caudal side of the MEA were more active, whereas during pulling the activity of these contacts decreased and contacts on the rostral side became more active, which is indicative of a spatial organization in the CST by function. It is not surprising to see a similar distribution in the 3-class scenario since the movement phases overlap with those of the 2-class case. The fact that flexion phase shares the characteristics of both extension and grasp movements indicates that this phase was more of a transient interval between the two movement phases. The classification results of the session being discussed, including the performance measures and confusion matrices, are summarized in Table 3.1.

Table 3.1 Classifications Results of a Representative Session (N=93 trials)

		2-class			**3-class**		
Accuracy		87%			62%		
		Predicted Class					
		Reaching	Pulling		Extension	Flexion	Grasp
True Class	Reaching	**85**	8	Extension	**53**	25	15
				Flexion	19	**59**	15
	Pulling	16	**77**				
				Grasp	11	20	**62**

One of the most important steps in designing a classification model is the selection of the classification algorithm in order to achieve the highest prediction accuracy. In general, an algorithm is chosen based on a set of criteria, such as prediction speed, memory usage, available processing power, the size of the feature set, the type (categorical vs numerical) and size of the dataset, and interpretability of the model (MATLAB 2017a). However, in most of the machine learning applications, a widely used practice is to compare multiple classification algorithms and pick the best performing technique in terms of accuracy and generalizability. Following this notion, we tested multiple techniques in both of our 2-class and 3-class classification paradigms. The prediction accuracies were computed by 5-fold cross validation for all available sessions of all animals. All classification algorithms (LDA, SVM, NB, KNN, and RF) performed similarly (Figure 3.9). Linear discriminant analysis (LDA) classifier performed slightly better than the others, and since it requires low processing power, runs faster, and works well with numerical data, we chose LDA as our predictive model.

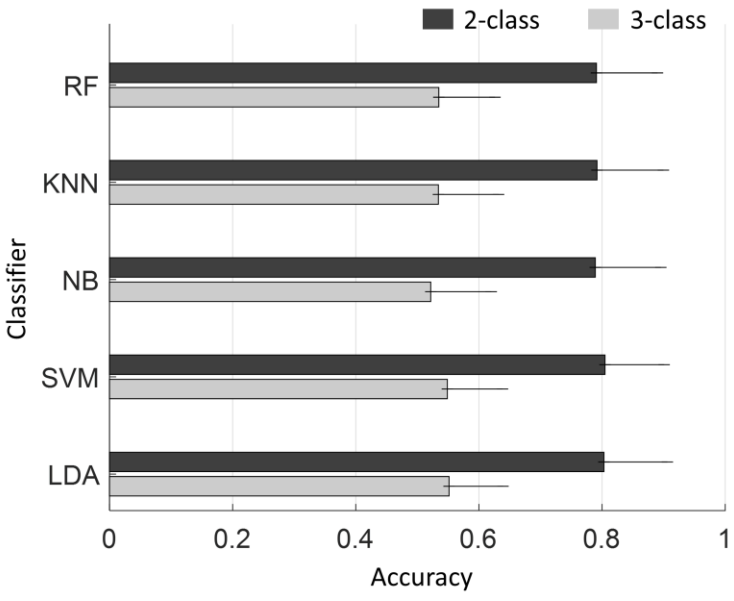

Figure 3.9 Comparison of the classification methods.

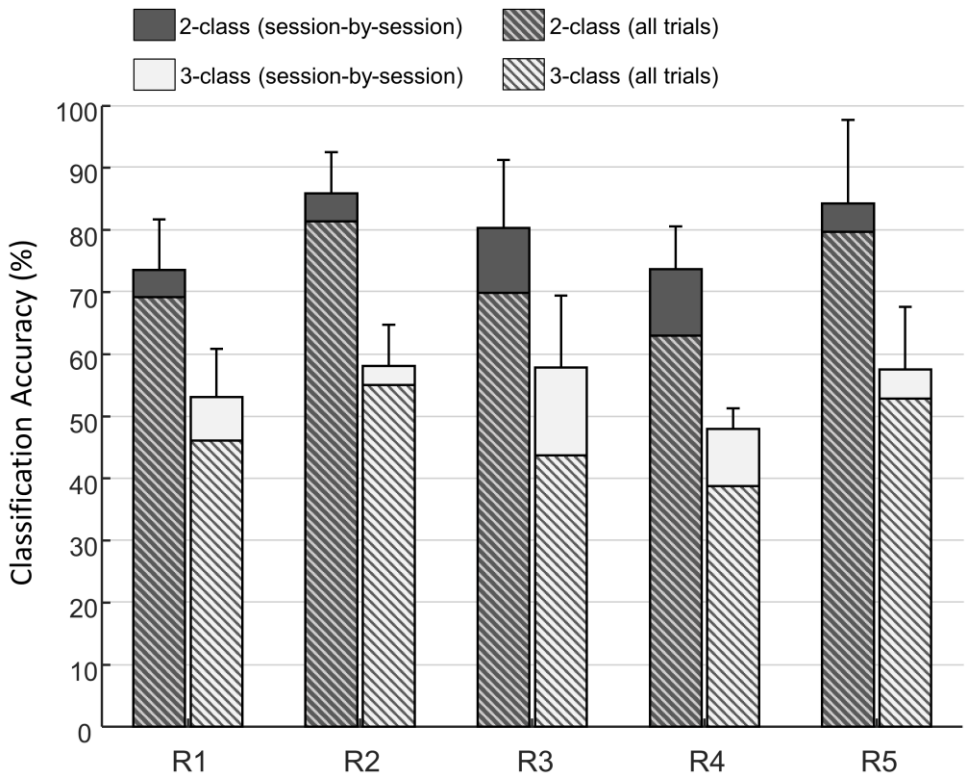

Figure 3.10 Group results of the classification analysis. Solid colored bars represent the mean accuracies when classification was performed session-by-session. Error bars indicate the standard deviations. Patterned bars represent the accuracies when all trials included in classification as a single group.

The ongoing cellular reactions in the electrode-tissue interface and the electrode micro-movements may lead to day-to-day variations in neural recordings, a phenomenon inherent to chronic neural electrode implants. To minimize the effects of day-to-day signal variations, we performed classification analysis on individual sessions. The group results are shown in Figure 3.10. The figure also includes results of classifications performed on all trials within each animal for comparison.

Table 3.2 Classification Results of all Sessions from All Rats

Rat	Session no	Days post-implant	Number of trials	Classification accuracy (%)	
				2-class	3-class
R1	1	15	78	69	49
	2	18	103	70	50
	3	20	102	72	46
	4	22	88	79	**64**
	5	26	93	**80**	62
	6	28	95	64	48
	Mean±STD		93±9	72±6	53±8
	All trials		552	69	46
R2	1	9	76	78	48
	2	13	114	75	52
	3	15	98	89	57
	4	21	100	92	60
	5	23	35	79	51
	6	26	93	**95**	**71**
	7	29	115	91	62
	8	34	94	89	67
	9	37	113	79	55
	10	40	106	88	55
	11	48	134	86	58
	12	56	123	90	61
	Mean±STD		100±26	86±6	58±7
	All trials		1196	81	55
R3	1	8	45	74	50
	2	14	19	71	57
	3	16	65	66	45
	4	19	109	85	52
	5	21	113	88	52
	6	24	79	72	58
	7	26	75	87	69
	8	31	69	**90**	**71**
	Mean±STD		72±31	79±9	57±9
	All trials		558	70	44
R4	1	7	43	70	47
	2	8	49	72	51
	3	12	86	72	43
	4	15	93	80	51
	5	19	102	68	48
	6	21	42	82	48
	7	25	75	**83**	**53**
	8	26	68	74	47
	9	29	89	62	45
	Mean±STD		72±23	74±7	48±3
	All trials		613	63	39
R5	1	6	46	89	57
	2	9	78	86	55
	3	13	97	82	55
	4	16	90	62	43
	5	20	82	95	70
	6	23	82	66	46
	7	27	80	**97**	67
	8	30	60	97	**68**
	Mean±STD		77±16	84±14	58±10
	All trials		584	80	53

We achieved classification accuracies as high as 97% for the 2-class and 71% for the 3-class paradigms. The fact that accuracies were not drastically reduced when classification was performed using all trials rather than session-by-session indicates that the day-to-day variations were present, but the recordings remained fairly stable during the course of the experiment. In general, 3-class classification performed poorly in comparison to the 2-class scenario, suggesting that the information captured by the electrode was insufficient to distinguish between a larger number of movement phases.

3.2.2 EMG Prediction

Data collection during behavior lasted 4 to 5 weeks, and we were able to record six experimental sessions (82 to 106 trials per session) with R1, four sessions (73-115 trials) with R2, five sessions (44-122 trials) with R3, nine sessions (42-119 trials) with R4, and seven sessions (43-112 trials) with R5. In R2, EMG wires were broken after the second week, and thus only the first four sessions were used in the regression analysis. As a representative session from R3, Figure 3.11 compares the linear predictions of all four muscle activities (dotted lines) to the actual EMG signals (solid lines) in multiple trials separated by dash lines. In this particular example, average trial length was 0.89±0.16 s with a training size of 36 and a test size of 8 trials. The prediction accuracies were found as CC=0.81 (R^2=0.64) for the biceps, CC=0.65 (R^2=0.42) for the flexors, CC=0.74 (R^2=0.53) for the triceps, and CC=0.69 (R^2=0.47) for the extensors. Representative predictions for the other rats are shown in Figure 3.12 through Figure 3.15.

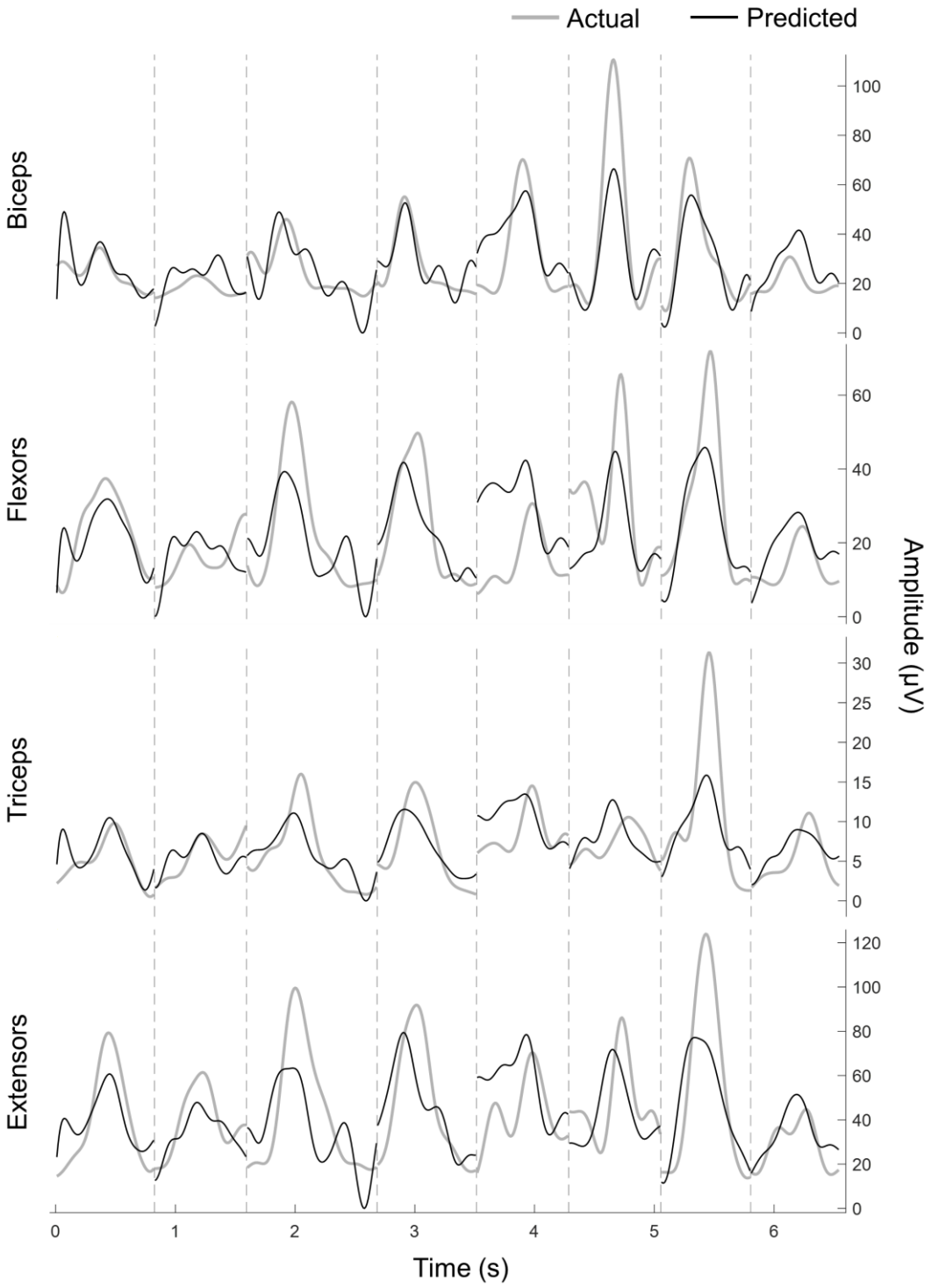

Figure 3.11 EMG predictions from R3. Actual (gray lines) and predicted (black lines) EMG signals during reach-to-pull task. The vertical dash lines separate individual trials. The prediction accuracy was calculated from the multiple trials treated as a continuous signal. CC=0.81 (R^2=0.64) for the biceps, CC=0.65 (R^2=0.42) for the flexors, CC=0.74 (R^2=0.53) for the triceps, and CC=0.69 (R^2=0.47) for the extensors.

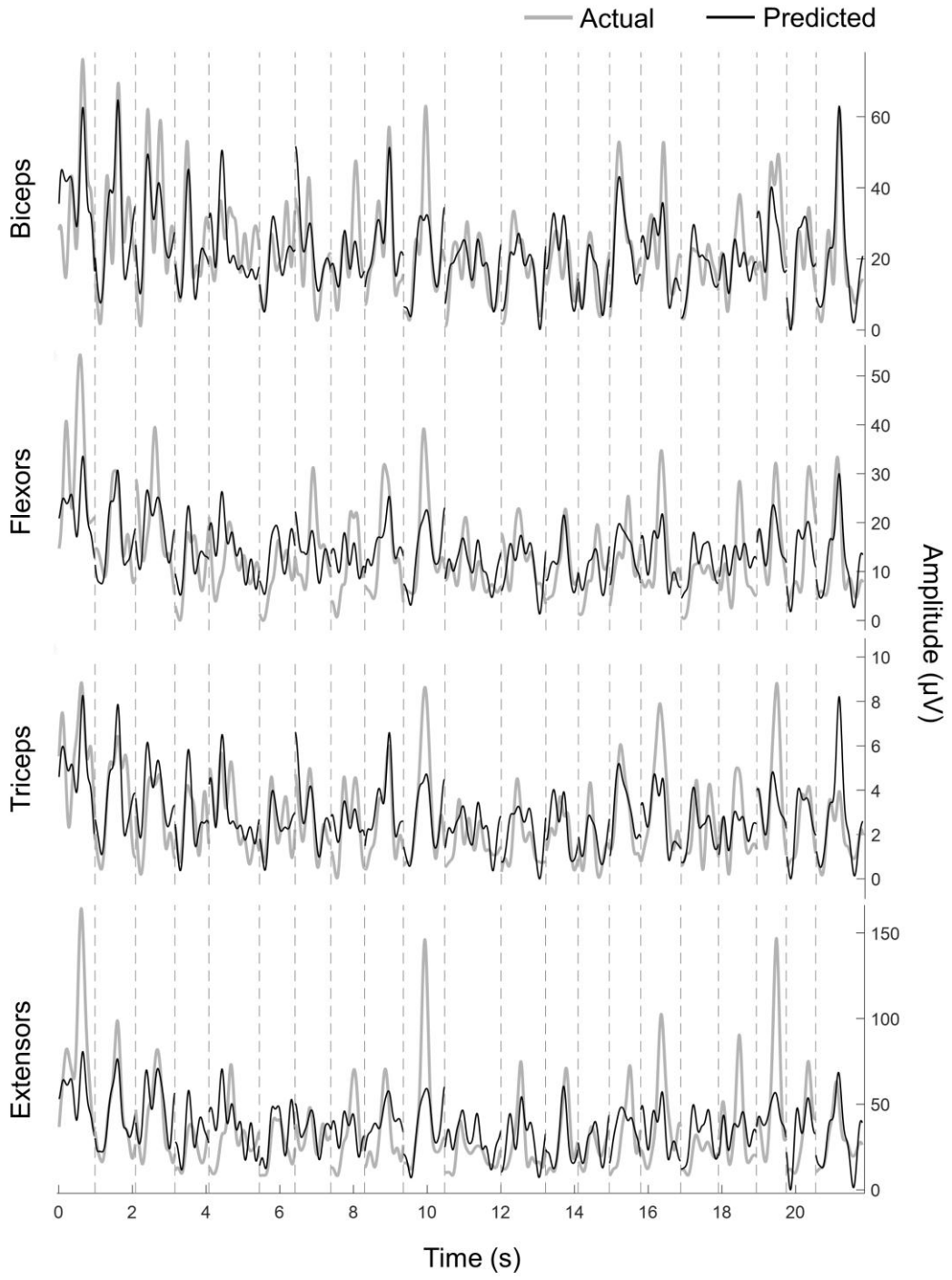

Figure 3.12 EMG predictions from R1. CC=0.80 (R^2=0.64) for the biceps, CC=0.66 (R^2=0.44) for the flexors, CC=0.73 (R^2=0.52) for the triceps, and CC=0.65 (R^2=0.41) for the extensors.

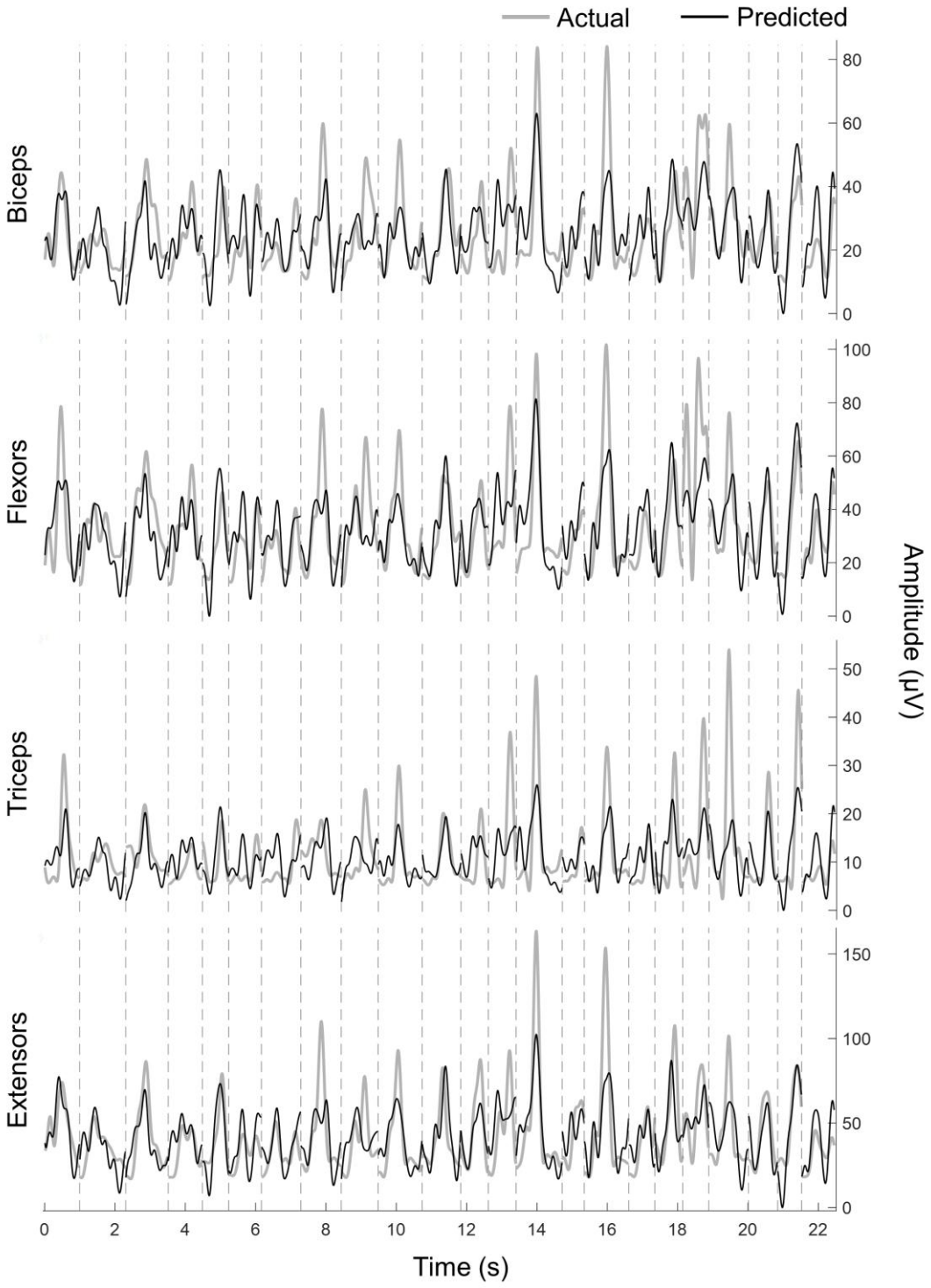

Figure 3.13 EMG predictions from R2. CC=0.71 (R^2=0.49) for the biceps, CC=0.71 (R^2=0.49) for the flexors, CC=0.62 (R^2=0.38) for the triceps, and CC=0.72 (R^2=0.51) for the extensors.

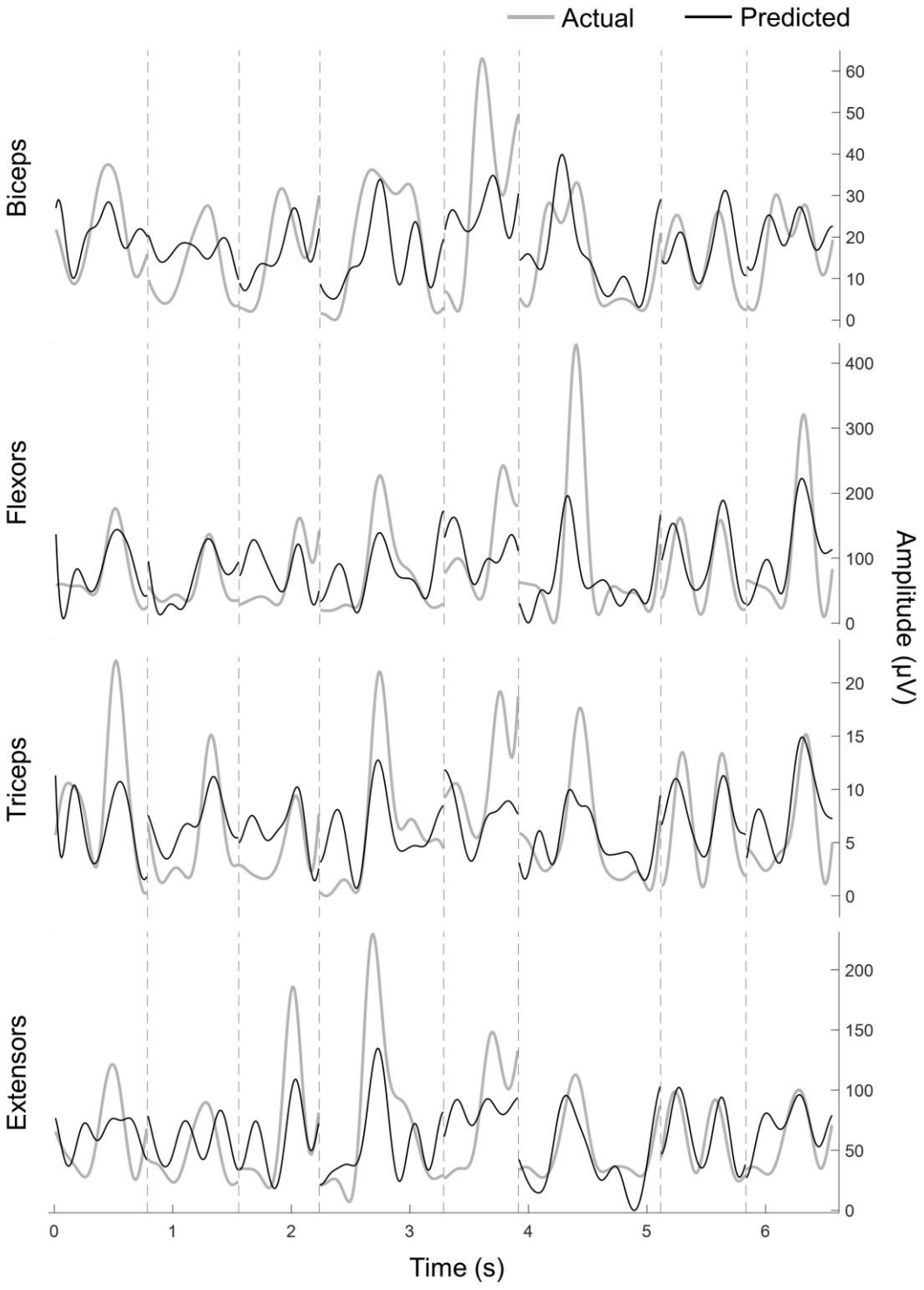

Figure 3.14 EMG predictions from R4. CC=0.61 (R^2=0.37) for the biceps, CC=0.59 (R^2=0.35) for the flexors, CC=0.69 (R^2=0.45) for the triceps, and CC=0.64 (R^2=0.40) for the extensors.

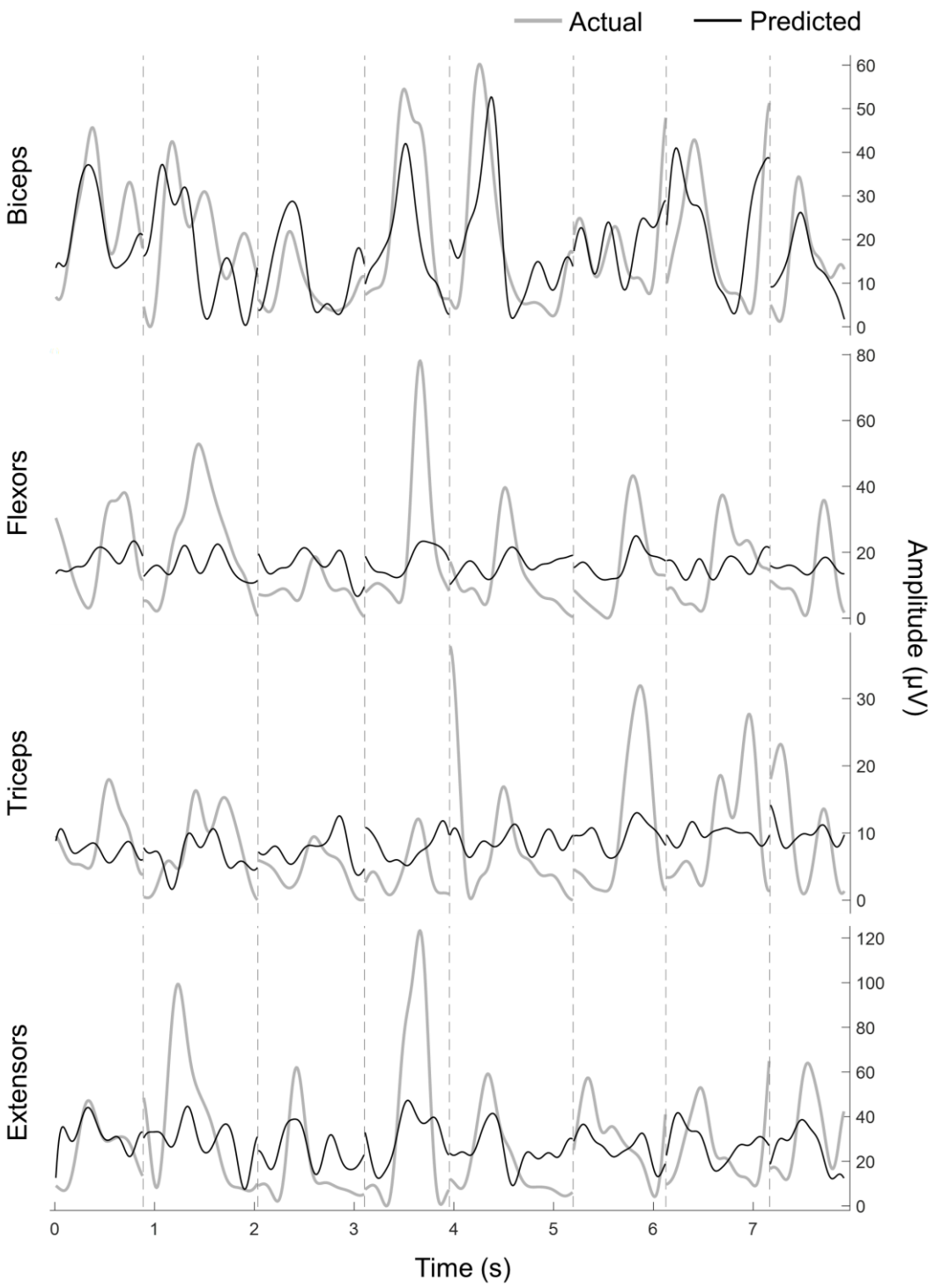

Figure 3.15 EMG predictions from R5. CC=0.65 (R^2=0.40) for the biceps, CC=0.49 (R^2=0.18) for the flexors, CC=0.37 (R^2=0.13) for the triceps, and CC=0.56 (R^2=0.27) for the extensors.

Figure 3.16 summarizes the means and standard deviations for all the predictions made from the data that was available from all rats. The highest average accuracy was achieved for biceps predictions in R1. Among all muscles, biceps had the highest predictions accuracies on average in all rats except R3, for which flexors attained the best prediction. When muscles were analyzed in groups, the extensor prediction was the highest for R3, the biceps and triceps predictions were the highest for R1, and the flexor predictions were the highest for R2. The predictions for R4 and R5 were not as good, and, in general, their average CCs were below 0.5 for all muscles. Even though the actual and predicted signals were correlated to a substantial degree, the R^2 values were drastically low especially for certain sessions and animals. The implications of high CC and low R^2 will be discussed in the next section.

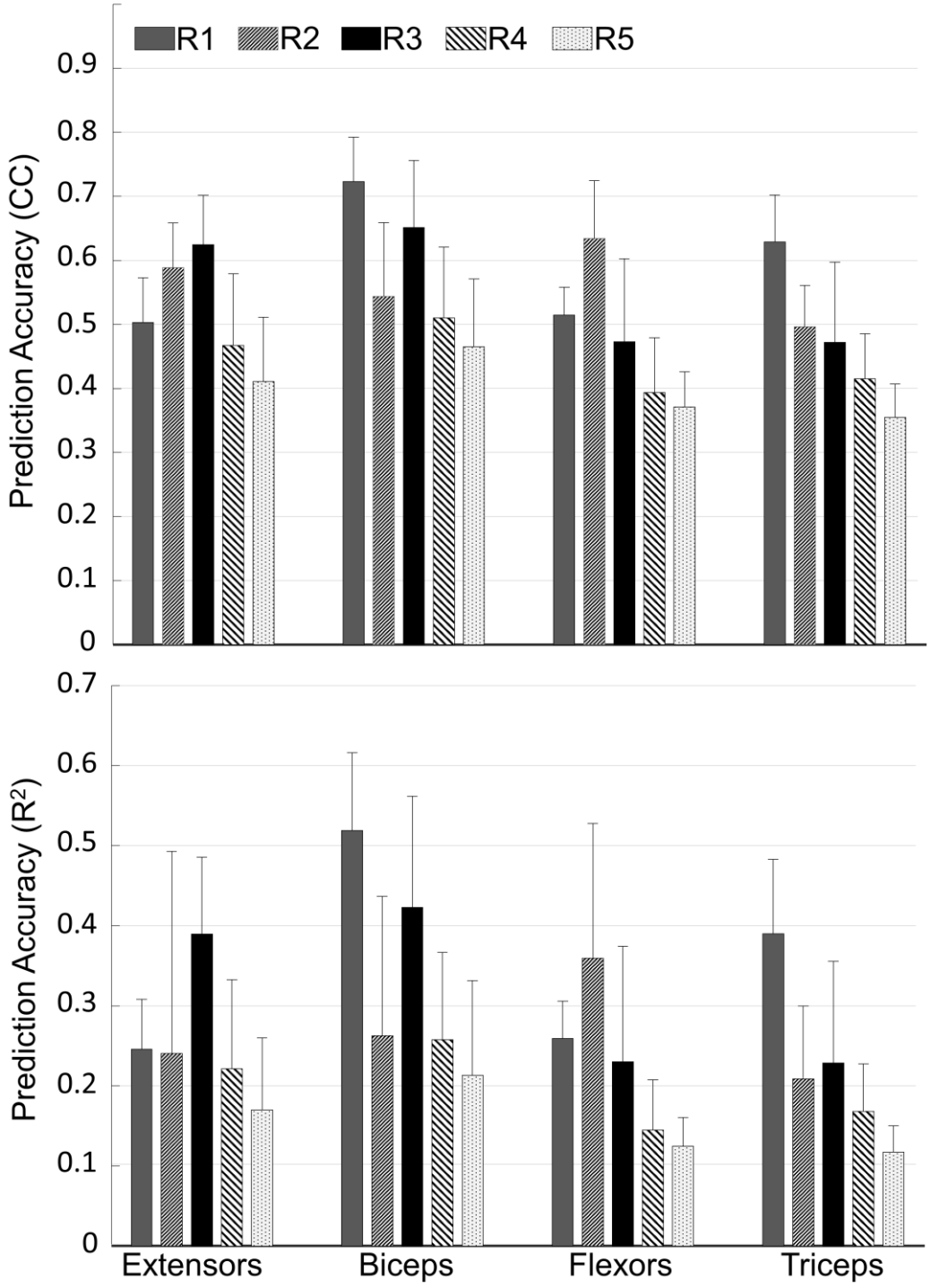

Figure 3.16 Mean±STD prediction accuracies of EMGs for all rats presented as CC (top) and R^2 (bottom) values.

Figure 3.17 illustrates the contributions made by LF and UF components to the prediction algorithm. The means and STDs were calculated over all session predictions for all animals. Models of R1 and R2 did not exhibit any preferences in assigning weights to the features; there was no significant difference between LF and UF contributions. However, the features in the LF band contributed significantly more in animals R3, R4, and R5 (paired t-test, $p<0.05$). The discrepancy might be due to different referencing techniques used in these two groups of animals as explained in the *Methods* section. We did not observe any significantly higher contributions made to the predictions by any single contact than others. The contributions were distributed more or less evenly among the contacts, indicating the fact that the first few principal components played a major role on the prediction algorithm.

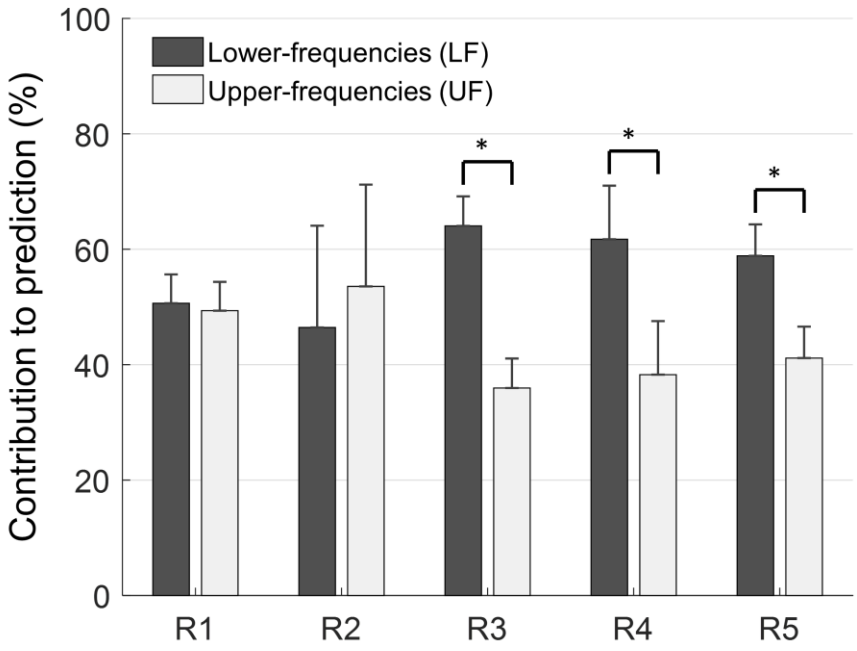

Figure 3.17 Percent contributions of LF and UF bands to the prediction for all rats.

The prediction accuracy varied depending on where the low-pass cutoff frequency was set while obtaining the EMG envelopes. Choosing a higher cutoff has the advantage

of increasing the EMG bandwidth and capturing fast changing muscle activities, and it is the preferred option for a high-speed neural interface. However, increasing the cutoff frequency may lead to decreased model performance since the linear decoder will most likely have a hard time explaining the variations in the dependent variable (EMG signals) using the limited information present in the independent variables (neural signals). Thus, it is important to reach a compromise between the prediction accuracy and the bandwidth while designing the low-pass filter. To measure the effect of the cutoff level, we run the prediction algorithm for a set of different low-pass filters and reported the average CC of all sessions within each animal (Figure 3.18). The best correlations were attained at 4Hz for all rats except R2. We chose 4Hz as the cutoff frequency in EMG predictions.

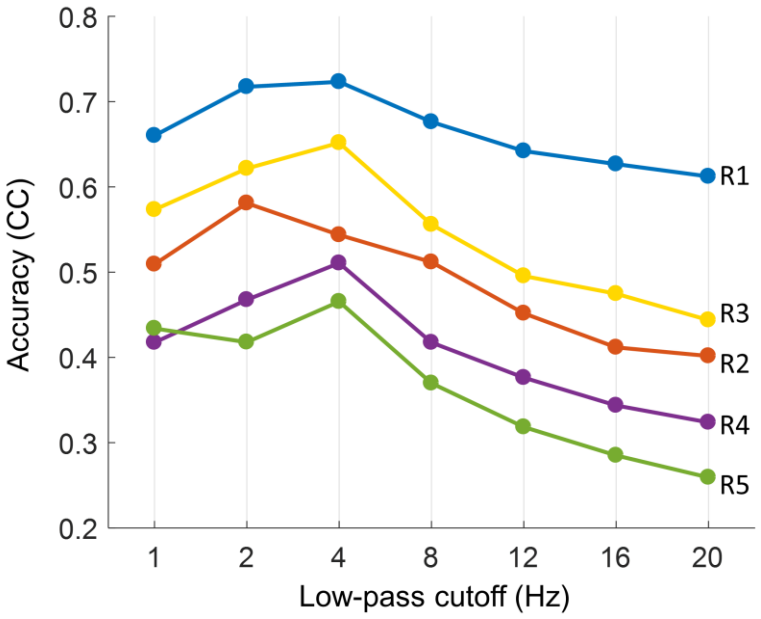

Figure 3.18 The prediction performance as a function of low-pass filter cut-off frequency. Data points show the mean prediction performance from all sessions in each rat. Highest predictions were at 4Hz for all rats except R2.

3.3 Confirmation of the Electrode Locations

EMG electrode locations were confirmed by electrical stimulation. The wrist extension and flexion were easily identifiable with distinct movements of the hand. Digits as well as the wrist were extended or flexed depending on the stimulation location. Threshold current intensities were higher for the biceps and triceps.

Figure 3.19 shows two samples of H&E stained transverse sections of the cervical spinal cords implanted with MEA electrodes in previous studies not reported in this study. The lesion in Figure 3.19a (2x magnification) demarcates where the electrode array was implanted in the dorsal white matter for a duration of 8 weeks. The image shows that the electrode was successfully positioned in the target area, the right side of the CST. The width of the lesion is less than 100 µm in this sample. Figure 3.19b (20x magnification) demonstrates a sample that was frozen together with the MEA and sectioned while the polyimide substrate was still inside the tissue (from R4, 5 weeks of implantation). The indentations at the contact locations near the tip can easily be identified.

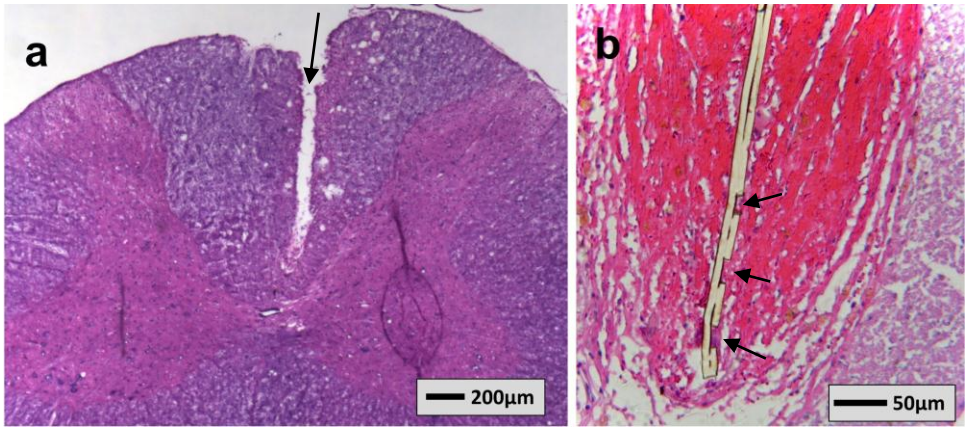

Figure 3.19 H&E stained transverse sections of cervical spinal cord. Left: the lesion demarcates the location of electrode array implanted in the dorsal column for 8 weeks. The void left after removing the electrode was noticeably narrow in this animal (indicated by an arrow). Right: a close-up picture of the actual electrode tip where indentations of the recording contacts can be seen in R4 (indicated by arrows). Bright red area shows the extent of tissue response for this particular implant.

3.4 Histological Examination

Figure 3.20 shows a LFB stained section of the spinal cord implanted with Utah microelectrode arrays from a previous study in our laboratory (Prasad & Sahin 2012b). The target regions in that study was the rubrospinal tract (RST), hence the location was the dorsolateral funiculus at the C5 level. Extensive tissue damage can be seen on the dorsal surface of the spinal cord caused by the weight of the electrode shank. Moreover, severe demyelination occurred as indicated by the light blue colored area that surrounds the electrode tips and extends beyond the gray matter nearing to the midline.

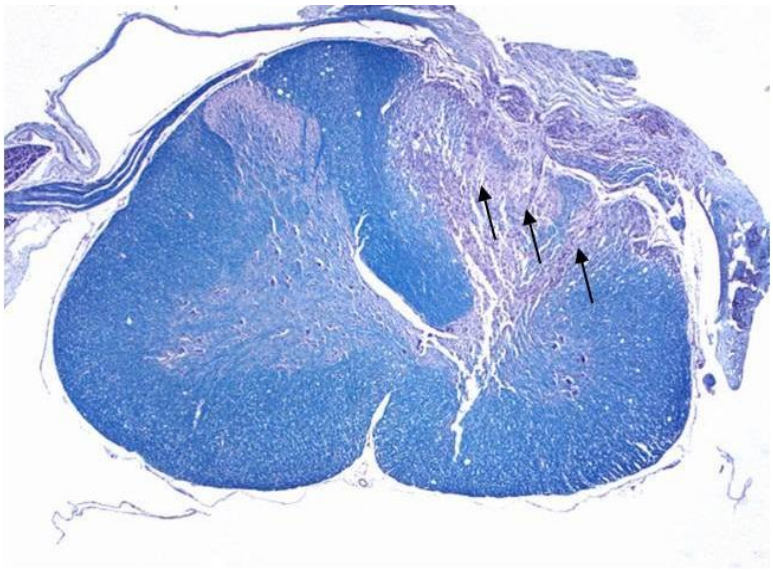

Figure 3.20 Utah array implanted spinal cord section (C5 level) stained with Luxol Fast Blue (4x magnification). Arrows show the traces left by the electrode tracks. Severe damage in the spinal cord and demyelination around the electrode tips can be seen.

Source: Prasad, A., & Sahin, M. (2012). Can motor volition be extracted from the spinal cord? Journal of Neuroengineering and Rehabilitation, 9(1), 41. https://doi.org/10.1186/1743-0003-9-41

The custom designed flexible polyimide based MEA used in this study, however, produced significantly less tissue response comparing to the silicon-based Utah MEA with a rigid shank. Figure 3.21 shows an LFB stained spinal cord section dissected from R2 after 8 weeks of implantation time. Demyelination was observed along the polyimide

substrate and under the collar that was placed above the dura, but the impacted area was small. A fragment of the Kapton© film (stopper) can be seen in the image. Figure 3.22 contains the same image at 4x magnification.

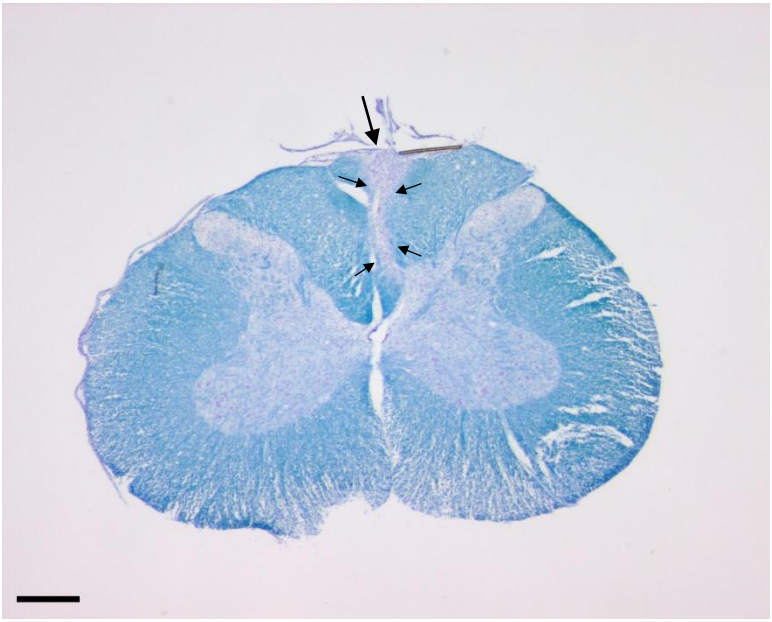

Figure 3.21 Transverse spinal cord section from R2 after 8 weeks implantation. The lesion indicated by light blue color in the right dorsal column (indicated by arrows) demarcates the electrode location. The demyelination inflicted by the flexible MEA was much smaller than that of the rigid shank arrays. A fragment of the Kapton© film that was used as a stopper is shown on the dorsal surface. The scale bar is 500µm.

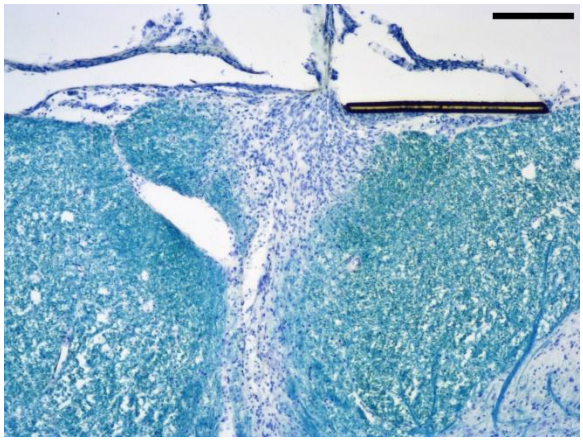

Figure 3.22 Transverse spinal cord section from R2 after 8 weeks implantation (4x magnification). The scale bar is 200µm.

Figure 3.23 shows an H&E stained section of the spinal cord dissected from R3 after 5 weeks of implantation time. The image also contains the fragments of polyimide ribbon cable and the Kapton© film (indicated by arrows) used as the stopper. The tissue response observed around the electrode (shown as the white space) has a width of 200-300 μm.

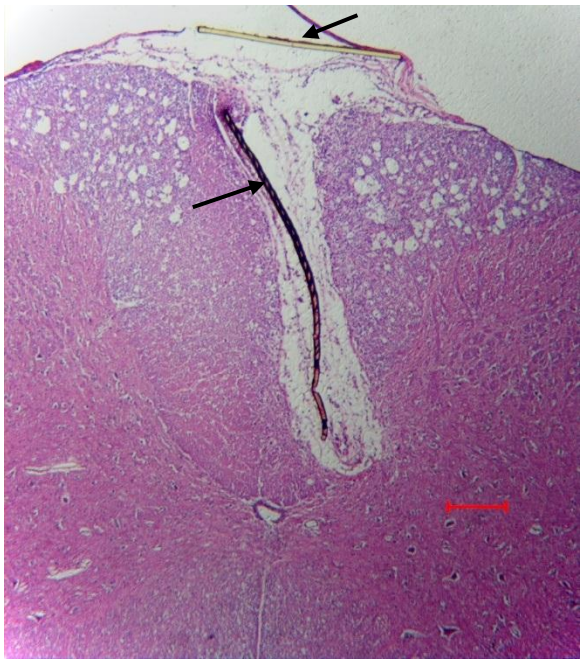

Figure 3.23 H&E stained section of the spinal cord dissected from R3 after 4 weeks of implantation time (4x magnification). The scale bar is 200μm.

An LFB stained section of the R4 spinal cord after 5 weeks of implantation time is shown in Figure 3.24. The section was taken while the electrode was intact and still inside the tissue. The yellow scale bar shows the length of the ribbon cable (1371 μm) that penetrated the spinal cord confirming our choice of implantation depth required to reach the CST. The width of the tissue response (marked by arrows and shown as the dark blue space between the electrode surface and the healthy white matter) varied between 100-150 μm (scale bar not shown). Figure 3.25 shows the same section at a magnification of 20x.

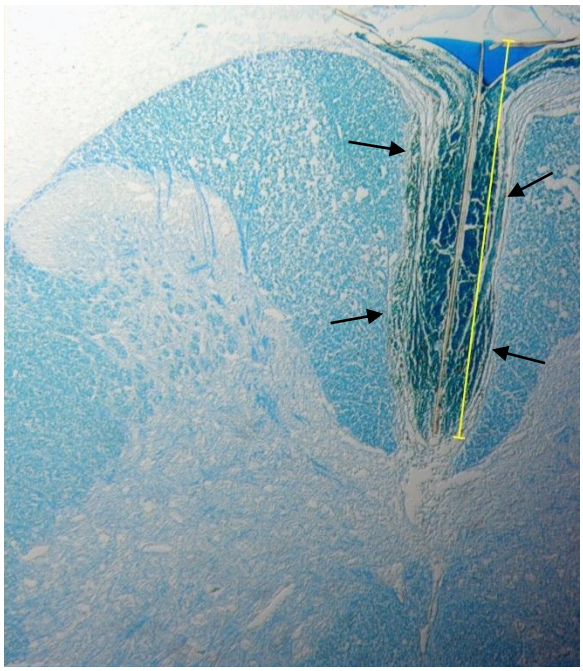

Figure 3.24 LFB stained section of the R4 spinal cord after 5 weeks of implantation time (4x magnification). The scale bar is 1371μm.

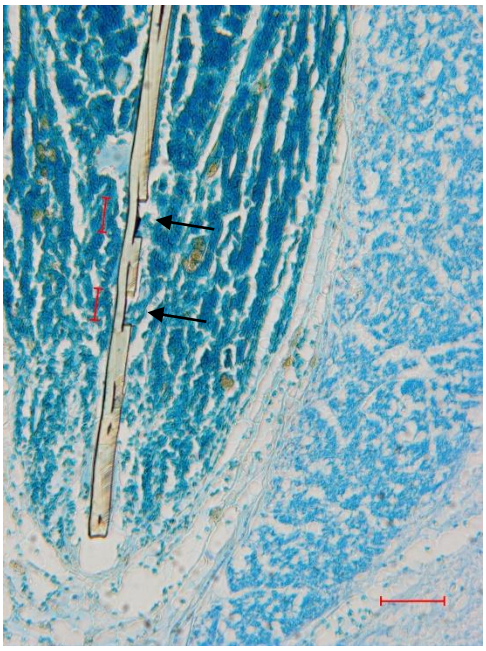

Figure 3.25 LFB stained section of the R4 spinal cord after 5 weeks of implantation time (20x magnification). Actual contact indentations (marked by arrows) can be seen. The scale bars are 27μm (vertical-top), 25μm (vertical-bottom), and 50μm (horizontal).

Figure 3.26 shows an H&E stained spinal cord section from R5 after 5 weeks of implantation. Tissue was deformed while transforming to the glass slide, nonetheless the tissue response can be identified. The purple dots around the electrode are the cell nuclei that most likely belong to astrocytes and microglia that surround the electrode material. The extent of the tissue response from the electrode surface to healthy fibers was ~200µm, a slightly larger value in comparison to the other rats.

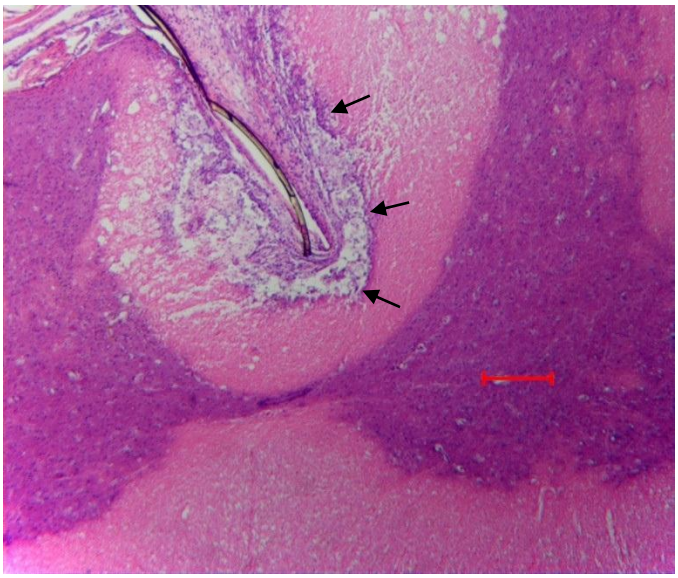

Figure 3.26 H&E stained section of a spinal cord dissected from R5 after 5 weeks of implantation time (4x magnification). The scale bar is 200µm. The boundary of the tissue response on the right side of the spinal cord is marked by arrows.

CHAPTER 4

DISCUSSION

We previously reported that the isometric forearm forces can be reconstructed from the CST activity in the rat via electrode arrays implanted at the cervical level (Guo et al. 2014). This study further demonstrates that the CST signals recorded using the same implant technique can predict the forelimb EMGs during dynamic movements. The CST signals were collected using a novel chronic implantation technique into the dorsal column that was developed in our laboratory with motivation to increase the long-term stability of neural recordings (Guo et al. 2014). Using this technique, we were able to record CST signals in freely moving rats up to 12 weeks of implantation time (not reported here). We have shown that the CST signals can be segregated into two or three different classes using the forelimb movement components as guidance criteria with 97% and 71% accuracies, respectively. We achieved predictions with correlation coefficients as high as 0.81 for the biceps EMG in individual sessions, although the average prediction accuracies varied considerably among rats. In general, the performance of EMG prediction was not as good as the CST classification based on movement phases, pointing towards the fact that CST signals were more efficient in decoding the movement phases rather than the instantaneous power of the EMGs as a function of time. In fact, comparison of the EMG envelopes and the predicted signals indicate that the CST signals were better at tracking the shape of the muscle activity waveforms rather than their absolute amplitudes, as reflected by high correlation coefficients but low R^2 values. The results of the present study corroborate our previous findings in which we have reported the ability to reconstruct forelimb kinematics,

such as hand velocity and elbow angle, using signals recorded from the CST by Utah arrays and micro-wires (Prasad & Sahin 2006).

4.1 EMG as an Output Parameter

While the exact cortical representation of the movement remains an active area of research, the fact that the central nervous system (CNS) has to transform the cortical signals into muscle activation patterns to generate a coordinated movement (Bizzi et al. 1991) led researchers to investigate the relationship between the cortical and the muscle activities. Kakei's experiments on trained monkeys showed that even though the majority of M1 cells correlated with the direction of the wrist movement, a significant number of cells showed "muscle-like" properties (Kakei et al. 1999). In general, half of the M1 neurons studied had movement-like characteristics, whereas the other half showed muscle-like behaviors (Scott 2008). The rate of information extracted from the neural signals has to be higher in order to predict fast changing movement parameters, such as the EMG. Cherian et al. have compared the performances of BCIs with kinetic (EMG) and kinematic (position and velocity) outputs using M1 recordings in monkeys (Cherian et al. 2011). The authors reported that within any given task, kinetic predictions were outperformed by the kinematic predictions. However, when they used decoders developed for specific tasks to predict signals recorded under different task conditions, authors observed that EMG decoders generalized better than kinematic decoders. Predicting EMG signals from neural activity has yet another practical implication in BCI studies (Nicolelis 2008). The decoded EMG signals can be used to directly control the electrical stimulations applied to the patient's own muscles and eliminate the need for external mechanical actuators.

4.2 Other EMG Prediction Studies

EMG prediction studies in the literature have exclusively used monkeys as the preferred animal model and they were primarily interested in the correlation of neuronal firings to the EMG envelopes. Morrow and Miller recorded from M1 neurons and several arm muscles of a monkey performing a grip task (Morrow & Miller 2003). Upon using multiple-linear regressions to fit the ensemble average of a neuronal discharge to different EMG signals, they were able to achieve an R^2 of 0.97 in their predictions using a group of 50 neurons. They concluded that a relatively small number of M1 neurons could provide sufficient information to reconstruct the EMG envelopes. Santucci *et al.* demonstrated that forearm EMG bursts can be predicted in monkeys from the ensemble activities simultaneously recorded from the primary motor, dorsal premotor, somatosensory, and posterior parietal cortices, which implies that the arm muscle activities can only be reconstructed by combining information from multiple brain regions (Santucci et al. 2005b). For biceps and triceps predictions respectively, they reported average correlation coefficients of 0.75 and 0.68 for one animal, and 0.80 and 0.73 for the other. Pohlmeyer *et al.* recorded M1 neuronal activity and EMG signals from hand and arm muscles of monkeys during button pressing and prehension tasks (Pohlmeyer et al. 2007). Authors showed that EMG envelopes of four forearm muscles can be predicted from optimally selected neuronal recordings with R^2 values in the range of 0.55-0.70, and prediction can be repeated for different trials and sessions up to two weeks. Shin *et al.* developed a method to predict muscle activities from electrocorticogram (ECoG) signals (Shin et al. 2012). In their method, ECoG signals were separated into different frequency bands, and the EMG signals were fitted using sparse linear regression. They reported CCs with a range of 0.55-

0.88 and concluded that online EMG prediction from ECoG recordings was feasible. To our knowledge, no previous attempts to predict muscle activities using the spinal cord signals have been reported in the literature.

We achieved EMG predictions that are consistent with the findings in the above-mentioned primate studies. However, the overall prediction performances of those studies were notably higher. The higher prediction accuracies in those studies can be attributed to the fact that the corticospinal tract neurons in primates have monosynaptic connections to the motor neurons in the ventral horn of the spinal cord. Furthermore, it is almost always possible to find neurons in the brain cortex whose activities are correlated with the selected movement parameter (Fetz 1992). However, selecting an optimal set of single units from a larger population presents complications in the long term. First of all, it is hard to track the same neurons for long periods of time since the electrode tips are susceptible to micro-motions and tissue reactions (Vadim S Polikov et al. 2005). Second, neurons may exhibit a task-dependent representation by switching their responses under varying task conditions (Kurtzer et al. 2005). In addition to that, in another study, authors have challenged the idea of approaching neuronal responses as "representations" by showing that the response patterns can change with respect to time, velocity, and distance (Churchland & Shenoy 2007). As in the case of "neuronal population activity" (Averbeck et al. 2006), the focus in BCI research has shifted to recording from multiple sources in order to compensate the variability in neural signals under changing conditions. In the spinal cord approach, we can assume that the multi-unit activities recorded from the descending pathways have representations from multiple motor-related areas of the brain since the axonal projections from those areas collectively travel through specific tracts of the spinal cord.

4.3 Availability of Proximal CST after Injury

SCCI method relies on the information extracted from the descending tracts that are proximal to the site of injury. Whether the CST neurons and axons survive the SCI has been a subject of debate for many years. Retrograde labelling studies on rats and monkeys reported apoptotic cell death in the CST neurons (Feringa et al. 1983; Feringa & Vahlsing 1985; Hains et al. 2003) and demyelination in the fiber tracts (Crowe et al. 1997) following the spinal cord injury. However, the follow up studies failed to show any significant loss in the CST neurons (McBride et al. 1990; Barron et al. 1988) and fibers in the medullary pyramid (Nielson et al. 2011). And notably, one particular study reported a decrease in the volume of the CST in rats 10 weeks after complete T9 transection, but observed no decrease in the number of axons in CST at C2 and T1 levels (Pruitt et al. 1988). These studies indicate that a substantial amount of CST axons do survive after the spinal cord injury.

CHAPTER 5

LIMITATIONS OF THE STUDY

Unlike the BCIs based on the population vector, the SCCI relies on the multi-unit activity from *en passant* axons with diameters less than 1 μm in the rat (Schreyer & Jones 1988) that are at a certain distance from the recording contacts. The MEA substrate had the smallest thickness (12 μm) that could withstand handling during implantation in order to minimize the tissue reaction due to electrode movements in behaving rats. Histological examinations revealed that the microglia-populated area extended 50 to 200 μm from the recording surface depending on the implant. These adverse effects lowered the signal-to-noise ratios and hindered the spatial selectivity of the signals. The information content available in the recorded CST signals may be very rich, however, the multi-channel electrode designs currently available do not allow access to majority of the descending activity without traumatizing the surrounding white matter. It is our belief that when such electrode technology is developed, multi-unit activity based approaches can provide more stable mappings over time than the single-spike recordings, between the descending spinal cord signals and the forelimb movement parameters (Kipke 2017).

Due to many developmental similarities between two species (Whishaw et al. 1992), the skilled reaching task in rats provides ample opportunities to assess the motor function and study the effects of neurological disorders in humans (Whishaw & Pellis 1990). Here, we used the reach-and-pull task to obtain the EMGs of forelimb muscles in a reproducible manner. Rats exerted pulling forces on a metal bar to receive a reward. Since the force is generated by co-activation of multiple muscles and modulated by joint

biomechanics, even slight variations in rat's posture, and relative positioning of the rat's body and forelimb can lead to significant difference in muscle activation patterns. Hence, the same force profile can be generated by different combinations of muscles in different trials. This dynamic relationship between the muscles and the behavior might have had an impact on the effectiveness of the predictive model. Furthermore, it has been argued that the nervous system is highly redundant consisting of 5 million descending motor fibers to control only 100-150 degrees of freedom of movement, (Neilson 1993). In particular, both corticospinal (CST) and rubrospinal tracts (RST) are involved in the control of distal muscles showing a functional redundancy in voluntary movement generation (Ghez 1975).

The CST and RST follow the lateral system that is involved in producing skilled forelimb movements and constitutes the main pathways for motor control in mammals (Gibson et al. 1985; Iwaniuk & Whishaw 2000). Electrophysiological lesion studies showed that the RST and CST have equal importance in forelimb control, although the relative contributions vary across species. Unilateral lesions to red nucleus, from which the RST originates, and medullary pyramid impaired the rotatory movements in rats including limb aiming, pronation and supination (Whishaw et al. 1998). Impaired arpeggio movement in some lesioning studies (Whishaw et al. 1998; Morris et al. 2011) suggest that the rat RST is more involved in proximal movements (e.g. hand rotation) than in digit use. The red nucleus receives projections from the cerebellum indicating that the RST plays a role in movement initiation and muscle coordination (Ghez & Kubota 1977; Lavoie & Drew 2002) as well as regulating the sensory feedback (Davis & Dostrovsky 1986). On the other hand, it has been shown that rat's ability to orient the paw for reaching was diminished following selective CST lesions, expressing a similarity to human CST injury

(Carmel et al. 2010). In summary, the current research suggests involvement of both the RST and CST in forelimb control, although the significance of each may be different depending on the specie and the behavioral task. Due to these variations in the neural mechanism of movement control, the signals responsible for the recorded EMGs may have not been captured by the spinal electrode in certain trials, leading to a poor performance of the predictive model. Moreover, spinal cord participates in movement generation via central pattern generators (CPGs) (Grillner & Zangger 1979) and muscles reflexes (Stein et al. 2000). Thus, the motor output from the spinal cord may be amplified locally based on the limb position and the external load. This suggests that the representation of movement in the descending tracts may be inadequate without inclusion of the sensory inputs. This conclusion is agreement with our previous observations (Guo et al. 2014) that the isometric force predictions produced progressively increasing errors when the forelimb was held at positions moving away from the original point used in the training data set.

CHAPTER 6

FUTURE DIRECTIONS

This study investigates the feasibility of a spinal cord computer interface that relies on the signals of the descending motor pathways. The signals in this study were recorded using an electrode array with a polyimide substrate, which was very flexible and durable for its size. However, tissue reactions induced by the electrode implant stretched up to 200 μm from the electrode surface and reduced the signal-to-noise ratio. The classification and prediction results showed that the information-rich content of the CST signals was not fully extracted; there is room for improvement to increase the SNR by reducing the tissue response. Recently studied carbon fiber micro-electrodes (CFMEs) are promising in terms of reducing the tissue damage upon and after insertion (Kozai et al. 2012; Patel et al. 2016) which makes them attractive alternatives to address the challenges we have faced in our research. Carbon fibers have been used in electrophysiological studies for their exceptional mechanical and electrical properties (Budai 2010). Chronically implanted CFMEs were proved to be reliable in single unit (Patel 2015) and multi-unit (Guitchounts et al. 2013) recordings. Our group has successfully demonstrated that custom made multi-channel carbon fiber electrodes can record spontaneous spinal cord activity in awake rats (Cetinkaya et al. 2017). Future work involves designing high-count (64-256 channels) carbon fiber electrodes to record from not only the CST but also the RST to increase the information content of recorded neural signals.

In this study, the Fourier analysis was used to transform the time signals into their frequency-band representations. The frequency spectrum was simply divided into two bands, lower and upper, and subsequent supervised learning algorithms employed these

two bands to associate CST signals with the model outputs. Using the Short-Time Fourier Transform (STFT) to account for both time and frequency domain information did not improve the performance, possibly because the Fourier transform decomposes the signal into weighted sinusoids at different frequencies instead of the underlying neural constituents, such as action potentials. Unlike the Fourier transformation, the "wavelet analysis" transforms the signal into scaled and translated versions of a base function, namely the mother wavelet, and it is an effective tool to analyze time-variant signals. Wavelet analysis provides a better localization of a certain event if the event sufficiently approximates the shape of the preferred wavelet. Therefore, we argue that describing signals using wavelets that best resemble the action potentials, or combined versions of actions potentials is more intuitive than decomposing them into sinusoidal constituents. Future work may include using wavelet analysis to extract neuronal features as inputs for the classification and prediction algorithms.

Finally, this study relied on the force data to detect movement phases and identify reproducible trials prior to data processing. However, a better approach would be using video recordings and image processing techniques. A synchronous video recording system with 3D tracking capability can provide higher accuracy in choosing similar trials while accounting for the external factors, such as animal's posture and forelimb position relative to rat's body.

REFERENCES

Alstermark, B., Lundberg, A. & Sasaki, S., 1984. Integration in descending motor pathways controlling the forelimb in the cat. 11. Inhibitory pathways from higher motor centres and forelimb afferents to C3-C4 propriospinal neurones. *Experimental Brain Research*, 56(2), pp.293–307.

Alstermark, B., Ogawa, J. & Isa, T., 2004. Lack of monosynaptic corticomotoneuronal EPSPs in rats: disynaptic EPSPs mediated via reticulospinal neurons and polysynaptic EPSPs via segmental interneurons. *Journal Of Neurophysiology*, 91(4), pp.1832–9.

Averbeck, B.B., Latham, P.E. & Pouget, A., 2006. Neural correlations, population coding and computation. *Nature Reviews Neuroscience*, 7(5), pp.358–366.

Barron, K.D. et al., 1988. Neurons of layer Vb of rat sensorimotor cortex atrophy but do not die after thoracic cord transection. *Journal Of Neuropathology And Experimental Neurology*, 47(1), pp.62–74.

Bizzi, E., Mussa-Ivaldi, F.A. & Giszter, S., 1991. Computations underlying the execution of movement: a biological perspective. *Science (New York, N.Y.)*, 253(5017), pp.287–91.

Brown, L.T., 1971. Projections and termination of the corticospinal tract in rodents. *Experimental Brain Research*, 13(4), pp.432–50.

Budai, D., 2010. Carbon fiber-based microelectrodes and microbiosensors. In *Intelligent and Biosensors*. InTech.

Cao, Y., Chen, Y. & DeVivo, M., 2011. Lifetime direct costs after spinal cord injury. *Topics in Spinal Cord Injury Rehabilitation*, 16(4), pp.10–16.

Carmel, J.B. et al., 2010. Feed-forward control of preshaping in the rat is mediated by the corticospinal tract. *The European Journal of Neuroscience*, 32(10), pp.1678–85.

Carmena, J.M. et al., 2003. Learning to control a brain-machine interface for reaching and grasping by primates. Idan Segev, ed. *PLoS Biology*, 1(2), p.E42.

Cetinkaya, E., Gok, S. & Sahin, M., 2017. Carbon fiber electrodes for recording spinal cord activity in rats. In *BMES Annual Meeting*. Phoenix, AZ.

Cherian, A., Krucoff, M.O. & Miller, L.E., 2011. Motor cortical prediction of EMG: evidence that a kinetic brain-machine interface may be robust across altered movement dynamics. *Journal of Neurophysiology*, 106(2), pp.564–575.

Churchland, M.M. & Shenoy, K. V., 2007. Temporal complexity and heterogeneity of single-neuron activity in premotor and motor cortex. *Journal of Neurophysiology*, 97(6), pp.4235–4257.

Crowe, M.J. et al., 1997. Apoptosis and delayed degeneration after spinal cord injury in rats and monkeys. *Nature Medicine*, 3(1), pp.73–76.

Davis, K.D. & Dostrovsky, J.O., 1986. Modulatory influences of red nucleus stimulation on the somatosensory responses of cat trigeminal subnucleus oralis neurons. *Experimental Neurology*, 91(1), pp.80–101.

Dunkerley, G.B. & Duncan, D., 1969. A light and electron microscopic study of the normal and the degenerating corticospinal tract in the rat. *The Journal of Comparative Neurology*, 137(2), pp.155–83.

Evarts, E. V, 1966. Pyramidal tract activity associated with a conditioned hand movement in the monkey. *Journal of Neurophysiology*, 29(6), pp.1011–27.

Evarts, E. V, 1968. Relation of pyramidal tract activity to force exerted during voluntary movement. *Journal of Neurophysiology*, 31(1), pp.14–27.

Feringa, E.R. & Vahlsing, H.L., 1985. Labeled corticospinal neurons one year after spinal cord transection. *Neuroscience Letters*, 58(3), pp.283–6.

Feringa, E.R., Vahlsing, H.L. & Smith, B.E., 1983. Retrograde transport in corticospinal neurons after spinal cord transection. *Neurology*, 33(4), pp.478–82.

Fetz, E.E., 1992. Are movement parameters recognizably coded in the activity of single neurons? *Behavioral and Brain Sciences*, 15, pp.679–690.

Georgopoulos, A.P. et al., 1982. On the relations between the direction of two-dimensional arm movements and cell discharge in primate motor cortex. *The Journal of neuroscience : the official journal of the Society for Neuroscience*, 2(11), pp.1527–37.

Ghez, C., 1975. Input-output relations of the red nucleus in the cat. *Brain Research*, 98(1), pp.93–308.

Ghez, C. & Kubota, K., 1977. Activity of red nucleus neurons associated with a skilled forelimb movement in the cat. *Brain Research*, 131(2), pp.383–388.

Gibson, A.R., Houk, J.C. & Kohlerman, N.J., 1985. Magnocellular red nucleus activity during different types of limb movement in the macaque monkey. *The Journal of Physiology*, 358, pp.527–49.

Gok, S. et al., 2015. *In vivo* impedance characterization of PEDOT:TFB coated and chronically implanted multi electrode arrays. *BMES Annual Meeting*. Tampa, FL.

Gorgels, T.G., 1990. A quantitative analysis of axon outgrowth, axon loss, and myelination in the rat pyramidal tract. *Brain Research. Developmental Brain Research*, 54(1), pp.51–61.

Gorgels, T.G. et al., 1989. A quantitative analysis of the development of the pyramidal tract in the cervical spinal cord in the rat. *Anatomy and Embryology*, 179(4), pp.377–85.

Grillner, S. & Zangger, P., 1979. On the central generation of locomotion in the low spinal cat. *Experimental Brain Research*, 34(2), pp.241–261.

Guitchounts, G. et al., 2013. A carbon-fiber electrode array for long-term neural recording. *Journal of Neural Engineering*, 10(4), p.46016.

Guo, Y. et al., 2014. Encoding of forelimb forces by corticospinal tract activity in the rat. *Frontiers in Neuroscience*, 8(8 MAY), p.62.

Hains, B.C., Black, J.A. & Waxman, S.G., 2003. Primary cortical motor neurons undergo apoptosis after axotomizing spinal cord injury. *The Journal of Comparative Neurology*, 462(3), pp.328–341.

Hochberg, L.R. et al., 2006. Neuronal ensemble control of prosthetic devices by a human with tetraplegia. *Nature*, 442(7099), pp.164–71.

Hyland, B.I. & Jordan, V.M.B., 1997. Muscle activity during forelimb reaching movements in rats. *Behavioural Brain Research*, 85(2), pp.175–186.

Illert, M. & Lundberg, A., 1978. Collateral connections to the lateral reticular nucleus from cervical propriospinal neurones projecting to forelimb motoneurones in the cat. *Neuroscience Letters*, 7(2–3), pp.167–172.

Iwaniuk, A.N. & Whishaw, I.Q., 2000. On the origin of skilled forelimb movements. *Trends in Neurosciences*, 23(8), pp.372–6.

Kakei, S., Hoffman, D.S. & Strick, P.L., 1999. Muscle and movement representations in the primary motor cortex. *Science (New York, N.Y.)*, 285(5436), pp.2136–9.

Kalaska, J.F. et al., 1997. Cortical control of reaching movements. *Current Opinion in Neurobiology*, 7(6), pp.849–59.

Kipke, D.R., 2017. CNS Recording: Devices and Techniques. In K. Horch & D. R. Kipke, eds. *Neuroprosthetics: Theory And Practice (Second Edition)*. Singapore: World Scientific, pp. 474–477.

Kozai, T.D.Y. et al., 2012. Ultrasmall implantable composite microelectrodes with bioactive surfaces for chronic neural interfaces. *Nature Materials*, 11(12), pp.1065–1073.

Kurtzer, I., Herter, T.M. & Scott, S.H., 2005. Random change in cortical load representation suggests distinct control of posture and movement. *Nature Neuroscience*, 8(4), pp.498–504.

Kuypers, H.G., 1981. Anatomy of the descending pathways. the Nervous System, Sect. 1, Vol. 2. In *Handbook of Physiology*. Hoboken, NJ, USA: John Wiley & Sons, Inc., pp. 597–666.

Kuypers, H.G.J.M., 1964. The descending pathways to the spinal cord, their anatomy and function. In *Progress in Brain Research*. Elsevier, pp. 178–202.

Lavoie, S. & Drew, T., 2002. Discharge characteristics of neurons in the red nucleus during voluntary gait modifications: A comparison with the motor cortex. *Journal of Neurophysiology*, 88(4), pp.1791–1814.

Lebedev, M.A. & Nicolelis, M.A.L., 2006. Brain–machine interfaces: past, present and future. *Trends in Neurosciences*, 29(9), pp.536–546.

Lee, B.H. et al., 2004. Injury in the spinal cord may produce cell death in the brain. *Brain Research*, 1020(1–2), pp.37–44.

Leenen, L.P. et al., 1985. A detailed morphometrical analysis of the pyramidal tract of the rat. *Brain Research*, 359(1–2), pp.65–80.

Leenen, L.P. et al., 1989. Differences in the fiber composition of the pyramidal tract in two- and 14-month-old rats. *Neuroscience*, 28(3), pp.635–43.

MATLAB, 2017a. Characteristics of classification algorithms. In *statistics and machine learning toolbox™ user's guide R2017b*. The Mathworks, Inc., Natick, MA, p. 1391.

MATLAB, 2017b. Estimates of predictor importance. In *statistics and machine learning toolbox™ user's guide r2017b*. The Mathworks, Inc., Natick, MA, p. 7211.

McBride, R.L. et al., 1990. Retrograde transport of fluoro-gold in corticospinal and rubrospinal neurons 10 and 20 weeks after T-9 spinal cord transection. *Experimental Neurology*, 108(1), pp.83–5.

Mediratta, N.K. & Nicoll, J.A., 1983. Conduction velocities of corticospinal axons in the rat studied by recording cortical antidromic responses. *The Journal of Physiology*, 336, pp.545–61.

Morris, R. et al., 2011. Impaired arpeggio movement in skilled reaching by rubrospinal tract lesions in the rat: a behavioral/anatomical fractionation. *Journal of Neurotrauma*, 28(12), pp.2439–51.

Morrow, M.M. & Miller, L.E., 2003. Prediction of muscle activity by populations of sequentially recorded primary motor cortex neurons. *Journal of Neurophysiology*, 89(4), pp.2279–88.

Nakajima, K. et al., 2000. Striking differences in transmission of corticospinal excitation to upper limb motoneurons in two primate species. *Journal of Neurophysiology*, 84(2), pp.698–709.

National Spinal Cord Injury Statistical Center, 2017. Facts and figures at a glance. *Birmingham, AL: University of Alabama at Birmingham*.

Neilson, P.D., 1993. The problem of redundancy in movement control: the adaptive model theory approach. *Psychological Research*, 55(2), pp.99–106.

Nicolelis, M., 2008. *Methods for neural ensemble recordings*, CRC Press/Taylor & Francis, New York, NY.

Nicolelis, M.A.L., 2003. Brain–machine interfaces to restore motor function and probe neural circuits. *Nature Reviews Neuroscience*, 4(5), pp.417–422.

Nicolelis, M.A.L. & Lebedev, M.A., 2009. Principles of neural ensemble physiology underlying the operation of brain-machine interfaces. *Nature Reviews. Neuroscience*, 10(7), pp.530–40.

Nielson, J.L., Strong, M.K. & Steward, O., 2011. A reassessment of whether cortical motor neurons die following spinal cord injury. *The Journal of Comparative Neurology*, 519(14), pp.2852–69.

de Noordhout, A.M. et al., 1999. Corticomotoneuronal synaptic connections in normal man: an electrophysiological study. *Brain : A Journal of Neurology*, 122 (Pt 7, pp.1327–40.

Paninski, L. et al., 2004. Spatiotemporal tuning of motor cortical neurons for hand position and velocity. *Journal of Neurophysiology*, 91(1), pp.515–32.

Patel, P.R., 2015. *Carbon Fiber Microelectrode Arrays for Neuroprosthetic and Neuroscience Applications* (doctoral dissertation). University of Michigan, Ann Arbor, MI.

Patel, P.R. et al., 2016. Chronic *in vivo* stability assessment of carbon fiber microelectrode arrays. *Journal of Neural Engineering*, 13(6), p.66002.

Pohlmeyer, E.A. et al., 2007. Prediction of upper limb muscle activity from motor cortical discharge during reaching. *Journal of Neural Engineering*, 4(4), pp.369–79.

Polikov, V.S., Tresco, P.A. & Reichert, W.M., 2005. Response of brain tissue to chronically implanted neural electrodes. *Journal of Neuroscience Methods*, 148(1), pp.1–18.

Polikov, V.S., Tresco, P.A. & Reichert, W.M., 2005. Response of brain tissue to chronically implanted neural electrodes. *Journal of Neuroscience Methods*, 148(1), pp.1–18.

Prasad, A. & Sahin, M., 2012a. Can motor volition be extracted from the spinal cord? *Journal of Neuroengineering and Rehabilitation*, 9(1), p.41.

Prasad, A. & Sahin, M., 2012b. Can motor volition be extracted from the spinal cord? *Journal of NeuroEngineering and Rehabilitation*, 9(1), p.41.

Prasad, A. & Sahin, M., 2010. Characterization of neural activity recorded from the descending tracts of the rat spinal cord. *Frontiers in Neuroscience*, 4, p.21.

Prasad, A. & Sahin, M., 2011. Chronic recordings from the rat spinal cord descending tracts with microwires. In *Proceedings of the Annual International Conference of the IEEE Engineering in Medicine and Biology Society, EMBS*. IEEE, pp. 2993–2996.

Prasad, A. & Sahin, M., 2006. Extraction of motor activity from the cervical spinal cord of behaving rats. *Journal of Neural Engineering*, 3(4), pp.287–292.

Pruitt, J.N., Feringa, E.R. & McBride, R.L., 1988. Corticospinal axons persist in cervical and high thoracic regions 10 weeks after a T-9 spinal cord transection. *Neurology*, 38(6), pp.946–50.

Santucci, D.M. et al., 2005a. Frontal and parietal cortical ensembles predict single-trial muscle activity during reaching movements in primates. *The European Journal of Neuroscience*, 22(6), pp.1529–40.

Santucci, D.M. et al., 2005b. Frontal and parietal cortical ensembles predict single-trial muscle activity during reaching movements in primates. *The European Journal of Neuroscience*, 22(6), pp.1529–40.

Saxena, T. et al., 2013. The impact of chronic blood-brain barrier breach on intracortical electrode function. *Biomaterials*, 34(20), pp.4703–13.

Schreyer, D.J. & Jones, E.G., 1988. Axon elimination in the developing corticospinal tract of the rat. *Developmental Brain Research*, 38(1), pp.103–119.

Schwartz, A.B. et al., 2006. Brain-controlled interfaces: movement restoration with neural prosthetics. *Neuron*, 52(1), pp.205–20.

Scott, S.H., 2008. Inconvenient truths about neural processing in primary motor cortex. *The Journal of Physiology*, 586(5), pp.1217–24.

Sengul, G. & Watson, C., 2014. Ascending and descending pathways in the spinal cord. In *The Rat Nervous System: Fourth Edition*. Oxford, UK, pp. 115–130.

Sengul, G. & Watson, C., 2015. Chapter 8 – ascending and descending pathways in the spinal cord. In *The Rat Nervous System*. Oxford, UK, pp. 115–130.

Serruya, M.D. et al., 2002. Instant neural control of a movement signal. *Nature*, 416(6877), pp.141–142.

Shin, D. et al., 2012. Prediction of muscle activities from electrocorticograms in primary motor cortex of primates M. Ptito, ed. *PLoS ONE*, 7(10), p.e47992.

Squire, L.R. et al., 2008. *Fundamental Neuroscience*, printed in China.

Stein, R.B., Misiaszek, J.E. & Pearson, K.G., 2000. Functional role of muscle reflexes for force generation in the decerebrate walking cat. *The Journal of Physiology*, 525 Pt 3(Pt 3), pp.781–91.

Suner, S. et al., 2005. Reliability of signals from a chronically implanted, silicon-based electrode array in non-human primate primary motor cortex. *IEEE Transactions on Neural Systems and Rehabilitation Engineering*, 13(4), pp.524–541.

Taylor, D.M., Tillery, S.I.H. & Schwartz, A.B., 2002. Direct cortical control of 3D neuroprosthetic devices. *Science (New York, N.Y.)*, 296(5574), pp.1829–32.

Truccolo, W. et al., 2008. Primary motor cortex tuning to intended movement kinematics in humans with tetraplegia. *The Journal of Neuroscience : the Official Journal of the Society for Neuroscience*, 28(5), pp.1163–78.

Vargas-Irwin, C.E. et al., 2010. Decoding complete reach and grasp actions from local primary motor cortex populations. *The Journal of Neuroscience : the Official Journal of the Society for Neuroscience*, 30(29), pp.9659–69.

Velliste, M. et al., 2008. Cortical control of a prosthetic arm for self-feeding. *Nature*, 453(7198), pp.1098–101.

Wessberg, J. & Nicolelis, M.A.L., 2004. Optimizing a linear algorithm for real-time robotic control using chronic cortical ensemble recordings in monkeys. *Journal of Cognitive Neuroscience*, 16(6), pp.1022–35.

Whishaw, I.Q., Gorny, B. & Sarna, J., 1998. Paw and limb use in skilled and spontaneous reaching after pyramidal tract, red nucleus and combined lesions in the rat: behavioral and anatomical dissociations. *Behavioural Brain Research*, 93(1–2), pp.167–83.

Whishaw, I.Q. & Pellis, S.M., 1990. The structure of skilled forelimb reaching in the rat: A proximally driven movement with a single distal rotatory component. *Behavioural Brain Research*, 41(1), pp.49–59.

Whishaw, I.Q., Pellis, S.M. & Gorny, B.P., 1992. Skilled reaching in rats and humans: evidence for parallel development or homology. *Behavioural Brain Research*, 47(1), pp.59–70.

Wolpaw, J.R. et al., 2000. Brain-computer interface technology: a review of the first international meeting. *IEEE transactions on rehabilitation engineering : a publication of the IEEE Engineering in Medicine and Biology Society*, 8(2), pp.164–73.

World Health Organization, 2016. Spinal cord injury. *World Health Organization*. Available at: http://www.who.int/mediacentre/factsheets/fs384/en/ [Accessed March 16, 2018].

Yang, H.-W. & Lemon, R.N., 2003. An electron microscopic examination of the corticospinal projection to the cervical spinal cord in the rat: lack of evidence for cortico-motoneuronal synapses. *Experimental Brain Research*, 149(4), pp.458–69.